DOI: 10.26599/FSHW.2026.9250925

Contents lists available at SciOpen

Food Science and Human Wellness

journal homepage: https://www.sciopen.com/journal/2097-0765

China Food Publishing Co.

Raspberry Ketone protects against type 2 diabetes mellitus-related lipotoxicity by suppressing ferroptosis via activation of the DJ-1/Nrf2 pathway

Yue Zhu [a, b, 1], Yuanbing Zhang [c, d, 1], Zhentao Li [a, 1], Jinna Xiao [a], Yaojun Cai [e], Chuanhua Feng [a], Ying Kong [a], Yanxia Jiang [e], Zhouyang Cheng [a, b], Jian Zhou [a], Jinfang Hu [a*], Zhengzheng Liao [a, f*]

[a] *Department of Pharmacy, The First Affiliated Hospital, Jiangxi Medical College, Nanchang University, Jiangxi 330006, China.*

[b] *School of Pharmacy, Nanchang University, Nanchang, Jiangxi 330006, China.*

[c] *Center for Experimental Medicine, The First Affiliated Hospital, Jiangxi Medical College, Nanchang University, Nanchang, Jiangxi 330006, China.*

[d] *Department of Pathology and Institute of Molecular Pathology, Jiangxi Provincial Key Laboratory for Precision Pathology and Intelligent Diagnosis, The First Affiliated Hospital, Jiangxi Medical College, Nanchang University, Nanchang, Jiangxi 330006, China.*

[e] *Department of Endocrinology and Metabolism, the First Affiliated Hospital, Jiangxi Medical College, Nanchang University, Nanchang, Jiangxi 330006, People's Republic of China*

[f] *State Key Laboratory of Food Science and Resources, China-Canada Joint Lab of Food Science and Technology (Nanchang), Nanchang University, Nanchang 330047, China*

ABSTRACT: Type 2 Diabetes Mellitus (T2DM) is a chronic metabolic disease, and dietary intervention is a fundamental strategy for its prevention. Raspberry ketone (RK) is a natural aromatic compound that comes from red fruits and berries, known for its hepatoprotective and hypoglycemic effects. However, the precise mechanism and direct target of RK in T2DM intervention remain unclear. This study aimed to elucidate how RK mitigates high-glucose-high-fat (HGHF)-induced lipotoxicity and ferroptosis, and to explore its potential implications for T2DM treatment. AML12 cell lines exposed to HGHF conditions and a T2DM mouse model induced by a high-fat diet (HFD) combined with streptozotocin (STZ) were used to investigate RK's protective effects. The results indicated that RK significantly alleviated lipotoxicity and ferroptosis in HFD/STZ-treated mice, as demonstrated by increased glutathione (GSH) and superoxide dismutase (SOD) expression, along with decreased malondialdehyde (MDA) levels. Furthermore, RK notably inhibited reactive oxygen species (ROS) production and apoptosis in AML12 cells under HGHF conditions. Mechanistically, RK activated the DJ-1/Nrf2 pathway, whereas DJ-1 knockdown using siRNA (siRNA-DJ-1) reversed these beneficial effects. Thus, DJ-1 is a crucial target of RK in AML12 cells and the T2DM mouse model. Consequently, RK represents a promising therapeutic approach for T2DM by targeting the DJ-1/Nrf2 pathway to reduce lipotoxicity and ferroptosis.

Keywords: Type 2 Diabetes Mellitus, Raspberry ketone, Parkinson disease protein 7, Nuclear Factor erythroid 2-Related Factor 2, ferroptosis, lipotoxicity

1. Introduction

[1]These authors contributed equally to this work
***Corresponding author**
Zhengzheng Liao, liaozhengzheng@ncu.edu.cn
Jinfang Hu, hujinfang333@126.com

Received 9 June 2025
Received in revised from 24 July 2025
Accepted 24 September 2025

Type 2 Diabetes Mellitus (T2DM) is a chronic metabolic disease increasingly prevalent among obese individuals and the aging population [1, 2]. With improved living standards and extended lifespan, the rising incidence of T2DM has become a significant societal burden. It is mainly characterized by hyperglycemia, hyperlipidemia, and insulin resistance. Its pathogenesis involves environmental and genetic factors, with islet β-cell dysfunction and death playing a crucial role in the disease progression and increased incidence observed in recent years [3]. Chronic hyperglycemia induces various complications, including kidney, eye, nervous, and cardiac injury. The failure to control high blood glucose and its complications over the long term raises the risk of physical disability and mortality [4]. Currently, effective clinical medications such as pioglitazone, metformin, and SGLT-2 inhibitors exist; however, they often exhibit limitations, including hepatic and renal toxicity or drug resistance after prolonged use. Thus, patients with diabetes and its complications endure significant physical and mental suffering, imposing a substantial financial burden on the public health system. As a result, developing safe and effective alternative treatments for diabetes is imperative. Food-derived medicinal products and their compounds hold unique advantages in treating T2DM, with extensive literature confirming their efficacy and indispensable role [5, 6].

As an alternative, food-derived medicinal products have been confirmed to help in blood glucose control and to enhance insulin sensitivity. Empirical evidence suggests that sufferers manage their diabetes symptoms by incorporating readily available and affordable food-derived medicinal products into their diet in developing and low-income countries [7]. Beyond their anti-diabetic properties, these food-derived medicinal products are recognized by many to provide additional nutrition intake and a lower incidence of side effects compared to pharmaceutical medications. Furthermore, nutrition intake for patients with diabetes symptoms limits the calorie and carbohydrate intake [8]. Medicinal herbs derived from food sources are generally rich in phytochemicals or bioactive compounds. For example, flavonoids, saponins and phenols from food sources have been confirmed to effectively control the blood glucose levels in patients with T2DM [9]. Therefore, bioactive compounds derived from food sources may contribute to the treatment of T2DM.

Abnormal glucose metabolism negatively impacts vital organs, including the liver, consequently affecting both insulin secretion and hepatic lipid metabolism. The liver pathology induced by diabetes begins with fat buildup in hepatocytes, leading to steatohepatitis and fibrosis around the hepatic portal area, along with pathological changes in blood markers and organ structure [10]. Emerging evidence has demonstrated that T2DM can induce significant alterations in liver volume, mediated through changes in hepatocyte quantity and apoptosis [11]. The key element in hepatocyte death is mainly due to the excessive production of free fatty acids (FFAs) within hepatocytes driven by abnormal lipid metabolism, which in turn impairs glucose metabolism and insulin sensitivity.

Elevated circulating FFAs trigger excessive ROS production by uncoupling the mitochondrial electron transport chain. This initiates a cycle of oxidative stress, culminating in β-cell dysfunction through DNA damage, lipid peroxidation, and activation of pro-apoptotic signaling cascades. Ferroptosis is a unique form of programmed cell death reliant on iron, characterized primarily by the intracellular accumulation of ROS,

which subsequently triggers lipid peroxidation and β-cell death in T2DM models [12, 13]. Excessive production of iron in liver could exacerbate lipid metabolism abnormalities and hepatocellular death, which in turn exacerbates the progression of T2DM. Existing research has extensively demonstrated that the suppression of the DJ-1/Nrf2 pathway significantly contributes to ferroptosis [14]. DJ-1 promotes Nrf2 release from the Keap1 complex, facilitating its entry into the nucleus and subsequent interaction with antioxidant response elements (ARE). This activity leads to the upregulated expression of antioxidant enzymes, notably glutathione peroxidase 4 (GPX4) and SLC7A11, thus mitigating ferroptotic damage [15]. In addition, downregulation of DJ-1 increases sensitivity in tumor cells toward ferroptosis-inducing compounds [16]. Moreover, substantial suppression of Nrf2 eliminates the protective efficacy of DJ-1 activators observed in db/db mouse models [17]. Additionally, knocking out the Nrf2 gene was associated with an increase in liver iron content [18]. Consequently, activating the DJ-1/Nrf2 signaling pathway might ameliorate insulin resistance and lipotoxicity in T2DM by inhibiting ferroptosis.

Raspberry ketone (RK), a naturally occurring compound, is present in red fruits and berries at a typical concentration of about 1-4 mg/kg. Accumulated research findings demonstrate that highly bioavailable RK can rapidly reach maximum absorption in the upper intestine and subsequently be metabolized into diverse beneficial metabolites in obese mice [19]. Furthermore, lipid-rich tissues, such as white adipose tissue (WAT), were confirmed to be a direct target of RK. In addition, RK, as a commercial dietary supplement, is recommended at maximum doses of 1400 mg per day, which substantially exceeds typical dietary intake to avoid adverse side effects [20]. Modern pharmacological research has found that RK provides benefits for weight loss, depression, cardioprotection, and hepatoprotection [21, 22]. Previous studies validated its protective effects against hyperglycemia and insulin resistance by modulating adipocytokines and oxidative stress in HFD-induced obese rats [23]. Xiong et al. identified RK as a potential α-glucosidase inhibitor [24], and Attia et al. reported its hypoglycemic effect by counteracting high-fat and high-glucose diet-induced reactions through the p-IRS-1/p-Akt/GLUT-4 pathway [25]. However, no studies have explored the precise mechanisms through which RK influences T2DM. Therefore, further research is necessary to determine the protective mechanisms of RK in T2DM.

In this investigation, both in *vivo* and in *vitro* experimental models were utilized to evaluate the effects of RK. The objective was to determine if RK mitigates ferroptosis through the suppression of ROS via activation of the DJ-1/Nrf2 axis. Additionally, understanding the protective effects of RK in T2DM could promote its further evaluation and potential as a safe, effective, and minimally toxic therapeutic alternative.

2. Materials and methods

2.1 Antibodies, Reagents and Media

RK (CAS: 5471-51-2, HPLC ≥ 99%, confirmed by HPLC) was procured from Macklin Biochemical Co., Ltd. (Shanghai, China). Antibodies targeting Bax, Bcl-2, HO-1, Nrf2, GPX4, NQO1, DJ-1 and SLC7A11 were produced from Cell Signaling Technology (Denver, MA, USA). Sigma Chemical Co. (MO, USA) supplied oleic acid-conjugated BSA solutions. Detection kits were purchased from Nanjing Jiancheng

Bioengineering Institute (Nanjing, China). PrimeScript FAST RT Reagent Kit with gDNA Eraser and TB Green Premix Ex Taq II were obtained from Takara Bio Inc. (Shiga, Japan). All additional chemical reagents involved in this research were acquired from Solarbio Science & Technology Co., Ltd. (Beijing, China).

2.2 Animals and Treatments

Five-week-old SPF-grade male C57BL/6 mice (Certificate NO. SCXK (Su) 2023-0009) were purchased from GemPharmatech Co., Ltd. (Nanjing, China). Experimental animals were maintained under strictly regulated conditions. Throughout the study period, food and water were provided ad libitum. All experimental protocols involving animals were approved by the Ethics Committee of the First Affiliated Hospital, Jiangxi Medical College, Nanchang University (Approval No. CDYFY-IACUC-202505GR044).

After a one-week acclimatization period, mice received a HFD for eight weeks to induce diabetes. This was followed by two intraperitoneal (i.p.) injections of streptozotocin (STZ; 100 mg/kg), dissolved in 0.1 M sodium citrate buffer (pH 4.5), administered at weeks 9 and 11. Two weeks later, fasting blood glucose (FBG) was measured, and mice exhibiting levels higher than 16.7 mmol/L were classified as successfully induced T2DM models. The animals were then randomly divided into five groups: control, model, RK low-dose (100 mg/kg), RK high-dose (200 mg/kg), and positive control (metformin, 300 mg/kg). Both RK and metformin were dissolved in a vehicle composed of 5% DMSO, 40% PEG300, 5% Tween-80, and 50% saline. The control and model groups received an equivalent volume of vehicle alone. The intervention lasted eight weeks; during this period, the control mice were provided with a normal diet, whereas the remaining groups continued receiving the HFD. Physiological indices, including body weight and FBG, were recorded biweekly to assess the therapeutic efficacy of RK.

2.3 Oral Glucose Tolerance Tests (OGTT)

After eight weeks of intervention, the experimental mice underwent fasting for 12 hours, followed by oral administration of glucose solution at 2 g/kg. Blood samples were subsequently drawn from tail veins at intervals of 0, 30, 60, 90, and 120 minutes post-administration, and glucose levels were determined with a glucometer. Data were analyzed by computing the area under the curve (AUC) across the 120-minute timeframe according to the following calculation:

$$AUC = (BG_{0min} + BG_{30min}) \times 0.5\ h \times 0.5 + (BG_{30min} + BG_{120min}) \times 1.5\ h \times 0.5$$

where BG_{0min}, BG_{30min}, and BG_{120min} represent blood glucose concentrations at 0, 30, and 120 minutes, respectively.

2.4 Assessment of Biochemical Indicators in Serum

The following day, the mice were euthanized, after which blood and hepatic tissues were rapidly harvested. Liver samples were preserved either by immediate freezing at -80 ℃ or by fixation in 4% paraformaldehyde. Whole blood samples underwent centrifugation at 3,000 × g for 10 minutes to collect the serum supernatants. Fe^{2+} (cat. CA1530, malondialdehyde (MDA, cat. BC0025), superoxide enzyme (SOD, cat. BC0170), glutathione peroxidase (GSH, cat. BC0205), triglyceride (TG, cat. A110-1-1), total cholesterol

(TC, cat. A111-1-1), high-density lipoprotein cholesterol (HDL-C, A113-1-1), and low-density lipoprotein cholesterol (LDL-C, A112-1-1) were analyzed using commercially available detection kits. The Fe^{2+}, MDA, SOD and GSH detection kits were obtained from Solarbio, Beijing, China. The TG, TC, HDL-C, and LDL-C detection kits were purchased from Nanjing Jiancheng Bio-engineering Institute, China.

2.5 Histopathological Examination and Oil Red O Staining

Liver tissue sections (5 μm thick) underwent hematoxylin and eosin (H&E) staining to assess general tissue morphology. Cryosections of liver tissue (8 μm thick) were stained with Oil Red O to evaluate lipid deposition, and images were captured utilizing a pathological slide scanner.

2.6 Immunohistochemical (IHC) Analyses

Paraffin-embedded tissue sections were baked, followed by deparaffinization and hydration. Antigen retrieval was achieved through heating at 96 ℃. Endogenous peroxidase was blocked by treating the sections with 3% H_2O_2 for 10 minutes at ambient temperature. After a 30-minute serum-blocking step, primary antibodies against DJ-1 (1:200 dilution) and GPX4 (1:100 dilution) were applied, and sections were incubated overnight at 4℃. Subsequently, sections were exposed to HRP-linked secondary antibodies, and staining was developed using DAB chromogen. Nuclear counterstaining was accomplished with hematoxylin. Following dehydration steps, the stained sections were mounted with neutral resin and protein expression was analyzed microscopically.

2.7 Cell Culture and Treatment

AML12 cells, acquired from Xiamen Immocell Biotechnology Co., Ltd. (Xiamen, China), were maintained in DMEM/F12 culture medium (Boster Biological Technology, Wuhan, China), supplemented with 10% fetal bovine serum, sodium pyruvate, penicillin-streptomycin, ITS supplement, and 40 ng/mL dexamethasone. Cell cultures were incubated under standard conditions of 37 ℃ and 5% CO_2 atmosphere. For viability assays, the 2×10^3 AML12 cells/well in 96-well plates were subsequently exposed for 24 hours to varying concentrations of RK (0-80 μmol/L), BSA (0-64 μmol/L), OA-bound BSA (0-0.4 mmol/L), glucose (GLU; 0-40 mmol/L), and metformin (Met; 0-2 mmol/L). Cell viability was then assessed by incubating cells with CCK-8 reagent (1:1000) for 2 hours in the dark. The absorbance was measured at 450 nm using a microplate reader. The RK was dissolved in DMEM/F12 culture medium containing 0.1% DMSO. Moreover, to identify the optimal treatment duration for OA (0.2 mmol/L) and GLU (10 mmol/L), cell viability was evaluated following exposure for 0, 3, 6, 12, 18, and 24 hours. The detection method was the same as mentioned above.

2.8 Oil Red O Staining of AML12 Cells

The AML12 cells (2×10^5 cells/well) were seeded in 6-well plates and pre-treated with RK (2.5, 5, 10 μmol/L) or Met (1 mmol/L) for 6 hours, followed by further incubation with OA (0.2 mmol/L) and GLU (10 mmol/L) for an additional 18 hours. Then, the cells were washed once with PBS and fixed with 4% paraformaldehyde (cat. P0099, Beyotime Biotech, Shanghai, China) for 10 min (cat. P0099, Beyotime

Biotech, Shanghai, China). After fixation, the cells were coated with dyeing detergent for 20 s, rinsed with PBS, stained using 1 mL Oil Red O staining solution (mixed with deionized water at a 3:2 ratio) for 20 min, and washed three times with PBS. The cells were then incubated with the hematoxylin staining solution (cat. C0107, Beyotime) to stain the nucleus. Finally, the lipid accumulation was observed using an inverted microscope (AxioVert.A1, Zeiss, Germany).

2.9 Determination of Biochemical Indicators in AML12 Cells

The AML12 cells were seeded at a density of 2×10^5 cells/well in a 6-well plate, followed by pre-treatment with RK (2.5, 5, 10 μmol/L) or Met (1 mmol/L) for 6 hours, and then incubated with OA (0.2 mmol/L) and GLU (10 mmol/L) for an additional 18-hour period. The cells were harvested and lysed with 100 μL cell lysis buffer (cat. P0013, Beyotime) in an ice bath. After centrifuged at 12,000 g for 10 min in 4 ℃, the supernatant was collected and the protein content was analyzed by a BCA protein quantification kit (cat. MA0082, Meilunbio, Dalian, China). Finally, the biochemical indicators of GSH, SOD, Fe^{2+}, MDA, and lacate dehydrogenase (LDH, cat. BC0685, Solarbio) were determined according to the operating instructions.

2.9.1 Estimation of reactive oxygen species (ROS) by flow cytometry

The intracellular ROS concentrations were determined utilizing 2',7'-dichlorofluorescein diacetate (DCFH-DA) fluorescent probe (cat. S0034S, Beyotime). Briefly, the AML12 cells were incubated in the DMEM/F12 culture medium and seeded in 6-well plates (2×10^5 cells/well) for 24 h. The next day, the cells were pretreated with RK (2.5, 5, 10 μmol/L) or Met (1 mmol/L) for 6 hours, followed by OA (0.2 mmol/L) and GLU (10 mmol/L) stimulation for 18 h. Then, cells were collected at a density of 1×10^6 per mL and incubated with 10 μmol/L DCFH-DA at 37 ℃ for 20 min in the dark. Finally, the samples were transferred to flow-specific tubes and determined by flow cytometry with an excitation wavelength of 485 nm and an emission wavelength of 538 nm. The raw data were analyzed by the Flow Jo 7.6 software (BD FACSCalibur; BD, NJ, USA).

2.9.2 Lipid Peroxides Assay

The intracellular lipid peroxides were determined utilizing a lipid peroxidation detection kit based on the BODIPY 581/591 C11 fluorescence probe (cat. S0034S, Beyotime). Briefly, the AML12 cells (2×10^5 cells/well) were seeded in 6-well plates and incubated with complete medium for 24 h. Then, the cells were pretreated with RK (2.5, 5, 10 μmol/L) or Met (1 mmol/L) for 6 hours, followed by OA (0.2 mmol/L) and GLU (10 mmol/L) stimulation for 18 h. The cells were collected (1×10^6 per mL) and incubated with 1 mL BODIPY 581/591 C11 fluorescence probe solution (2 μmol/L, diluted with PBS at a ratio of 1:1000) for 20 min in a 37 ℃ incubator. After washing twice with PBS, 2 mL PBS was added to observe using a fluorescence microscope (Primo vert iLED, Zeiss).

2.9.3 Detection of Mitochondrial Membrane Potential Using JC-1

The mitochondrial membrane potential is one of the main biomarkers used to evaluate mitochondrial dysfunction. The mitochondrial membrane potential was detected by the JC-1 (cat. 2005, Beyotime). The

AML12 cells (2×10^5 cells per well) were seeded for 24 h in the 6-well plates. The next day, RK (2.5, 5, 10 μmol/L) or Met (1 mmol/L) were co-cultured with AML12 cells for 6 hours and then added OA (0.2 mmol/L) and GLU (10 mmol/L) for an additional 18 h. After being washed twice with PBS and digested with trypsin, the suspension was collected in a 1.5 mL EP tube and subsequently centrifuged at 2000 g for 10 min. The residue was added 0.5 mL JC-1 working solution (50 μL 200×JC-1 stain+ 8 mL dd H_2O + 2 mL JC-1 buffer) and co-incubated at 37 ℃ in an incubator for 20 min. Then, the AML12 cells were washed three times with PBS and resuspended in PBS (200 μL). Finally, the samples were subjected to flow cytometric assessment.

2.9.4 Annexin V/PI Apoptosis Assay

Apoptosis was detected by an Annexin V-FITC/PI Apoptosis Detection Kit (cat. MA0220, Meilunbio, Dalian, China). Briefly, the cells were collected, washed three times with PBS, and then resuspended in 100 μL 1×Binding Buffer (diluted with PBS, 1×10^5 cells/mL) containing 5 μL Annexin V FITC and 5 μL PI, and co-incubated in the dark for 15 min at 25 ℃. The samples were detected by a Multicolor Flow Cytometry (NovoCyte D3000, Agilent, USA). The FI-TC positive events represent apoptotic cells, and the ratio of cell apoptosis was the sum of the Q2 and Q3 regions.

2.9.5 Immunofluorescence (IF) Analysis

After completion of treatments, AML12 cells (1×10^5 cells/well) were permeabilized with 0.5% Triton X-100 for 60 min, rinsed with PBS, and blocked using a 3% BSA solution. The cells were incubated overnight at 4 ℃ with primary antibodies against Nrf2 (1:200) and DJ-1 (1:100), respectively. Following multiple washes, a secondary antibody was applied at ambient temperature for one hour. The cells were then counterstained with DAPI for nuclear visualization, mounted using an anti-fade medium, and analyzed for comparative fluorescence intensity using a laser scanning confocal microscope (Nikon eclipse-E, JPN).

2.10 Small Interfering RNA (siRNA) Transfection

AML12 cells were subjected to DJ-1 knockdown *via* transfection with specific siRNAs synthesized by Zolgene Biotechnology Co., Ltd. Cells at approximately 50% confluence were transfected with the siRNAs for 24 hours, and Western blot and RT-qPCR analysis were performed to validate the efficiency of DJ-1 suppression. The target sequences were as follows: DJ-1-siRNA1, CCAAAGGAGCAGAGGAGAUTT, AUCUCCUCUGCUCCUUUGGTT; DJ-1-siRNA2, GGAAAGACAUGGCCAACCATT, UGGUUGGCCAUGUCUUUCCTT; DJ-1-siRNA3, GCAGUGUAGCCGUGAUGUATT, UACAUCACGGCUACACUGCTT; DJ-1-siRNA NC, UUCUCCGAACGUGUCACGUTT, ACGUGACACGUUCGGAGAATT; DJ-1-siRNA FAMNC, UUCUCCGAACGUGUCACGUTT, ACGUGACACGUUCGGAGAATT; DJ-1-siRNA positive control, UUGAUGACAAGCUUCCCAUUCUTT, AGAAUGGGAAGCUUGUCAUCAATT.

2.11 Western blot Analysis

After the experiment, Protein samples from AML12 cells and liver tissues were extracted using RIPA buffer containing 1% protease and phosphatase inhibitor cocktails (1:10) in an ice-water bath. The lysates of

cells and liver tissues were centrifuged at 12,000 g for 10 min at 4 ℃, and the supernatant was transferred to a 1.5 mL tube. Then, the quantification of proteins was performed using a BCA assay (cat. MA0082, Meilunbio, Dalian, China), and the protein concentration was adjusted to the same level using the RIPA buffer. Subsequently, protein samples underwent electrophoresis on 8-12% SDS-PAGE gels and were transferred onto PVDF membranes. The membranes were blocked with 7.5% skim milk and incubated overnight at 4 ℃ with primary antibodies against DJ-1 (1:5000), NRF2 (1:2000), HO-1 (1:1000), NQO-1 (1:1000), GPX4 (1:2000), SLC7A11 (1:800), BAX (1:1000), Bcl2 (1:1000), and β-actin (1:5000). After triple washes with TBST, the membranes were incubated at 25 ℃ with secondary antibodies (1:10000) for two hours. Visualization of immunoreactive bands utilized enhanced chemiluminescence (ECL) reagent on a UVP ChemStudio 515 imaging system (Jena, Germany).

2.12 Immunoprecipitation (IP) Assay

HEK293T cells were cultured in 10-cm dishes and transfected with pCMV-SLC7A11(human)-3×HA-Neo and pECMV-3×FLAG-NRF2 plasmids (Miaoling Biotechnology, China) using polyethylenimine (Sigma). IP assays were performed to evaluate interactions between SLC7A11 and Nrf2. Approximately 5×10^6 cells (per dish) were harvested 48 h after transfection and washed twice with cold PBS. Cells were lysed in 500 μL of ice-cold TNE buffer (50 mmol/L Tris-HCl, pH 7.4; 150 mmol/L NaCl; 1 mmol/L EDTA; 1% NP-40) supplemented with a protease inhibitor cocktail (MCE). Lysates were clarified by centrifugation at 12,000 × g for 15 min at 4 ℃, and the supernatants were collected. For each sample, 10% (50 μL) of the clarified lysate was saved as input, while the remaining supernatant was incubated with anti-FLAG magnetic beads (Sigma-Aldrich) overnight at 4 ℃ with gentle rotation. The beads were then washed three times with cold TNE buffer, and bound proteins were eluted by boiling in 1 × SDS loading buffer for 10 min. Eluted proteins (IP) and input fractions were resolved by SDS-PAGE and transferred to PVDF membranes, followed by Western blot. Immunoblotting was performed with anti-HA antibody (CST, USA) to detect SLC7A11 and anti-FLAG antibody (Sigma-Aldrich) to confirm NRF2.

2.13 Protein Structure Prediction and Visualization

Amino acid sequences of human SLC7A11 and NRF2 were retrieved from the UniProt database. Protein-protein interactions were predicted using AlphaFold3, a deep-learning-based prediction tool. Structural features and potential interaction sites between SLC7A11 and NRF2 were visualized and analyzed using PyMOL.

2.14 Reverse Transcription-Quantitative real-time PCR (RT-qPCR)

Total RNA was isolated from tissues (100 mg) and AML12 cells (2×10^6 cells/well) using Trizol reagent (1 mL, Tiangen, Inc., Beijing, China) for 5 min at 4 ℃, followed by 200 μL chloroform for 5 min. After centrifuging at 10,000 g for 15 min at 4 ℃, the supernatant was mixed with 0.5 mL isopropanol by vortexing for 30 s, incubated for 15 min and subsequently centrifuged at 13,000 g for 15 min at 4 ℃. The RNA pellet was washed with 1 mL 75% ethanol, followed by centrifugation at 8,000 g for 5 min at 4 ℃. After

air-drying, the pellet was resuspended in 20 μL RNase-free water to obtain purified RNA. The concentration and purity of RNA were measured using NanoDrop™ 8000 Microvolume UV-Vis Spectrophotometer (Thermo Fisher Scientific, USA). Finally, the purified RNA was reverse transcribed into cDNA employing a reverse transcription kit (TaKaRa, Beijing, China). RT-qPCR assays were executed with NovoStart® SYBR qPCR SuperMix Plus on a CFX96 Touch Real-Time PCR Detection System (Bio-Rad, USA). Relative expression levels were quantified by the $2^{-\Delta\Delta CT}$ method and normalized against β-actin. Specific primer sequences are detailed in Table 1.

Table 1 Primers for qPCR analysis to detect mRNA levels.

Gene	Forward primer sequence	Reverse primer sequence
NQO-1	5'-CCGCATTCGTCTCTTGTCCG-3'	5'-CGAAGTAACACAATGGGCTTGG-3'
HO-1	5'-CAGAGCCGTCTCGAGCATAG-3'	5'-CAAATCCTGGGGCATGCTGT-3'
DJ-1	5'-GCCAAAGTCCTAGGAAACGC-3'	5'-CCGGGTTGAAAGGTTCAGGA-3'
Nrf2	5'-GCCACCTTTTGACAGTGATG-3'	5'-GTGCTGCTGCGAGATTTGAA-3'
GPX4	5'-AGCCAGAGTCCTTCAGAGAGA-3'	5'-GCCACTCCTTCTGTGACTCC-3'
β-actin	5'-CGCAGCCACTGTCGAGTC-3'	5'-TCATCCATGGCGAACTGGTG-3'

2.15 Cellular Thermal Shift Assay (CETSA)

AML12 cell lysates were treated with 10 μmol/L RK or an equal volume of DMSO at 25 ℃ for 60 min. The lysates were then equally divided into seven portions and heated at temperatures of 40, 45, 50, 55, 60, 65, and 70 ℃, followed by stabilization at 25 ℃ for 3 min. Supernatants were collected after heating and analyzed by Western blot.

2.16 Drug Affinity Responsive Target Stability (DARTS)

AML12 cell lysates (600 μL) were mixed thoroughly with 60 μL of 10× TNC buffer, followed by protein quantification *via* the BCA method. The prepared lysates were equally split into two groups, each treated at 25℃ for 1 hour with either RK or DMSO. Each sample was further split into six aliquots, incubated with protease enzyme at ratios of 0, 1:100, 1:500, 1:1000, 1:5000, and 1:10000 for 30 min at 25 ℃, and subsequently analyzed by Western blot.

2.17 Statistical Analysis

Data represent at least three replicates from independent experiments and were statistically analyzed by one-way ANOVA, with subsequent post hoc Student-Newman-Keuls tests using SPSS version 22.0. Results are presented as mean ± standard error, with statistical significance set at $P < 0.05$.

3. Results

3.1 RK Alleviated Symptoms in T2DM Mice

Previous studies indicated that RK could mitigate clinical features of T2DM. Consistent with these findings, our results demonstrated RK's beneficial effects in T2DM mice. As shown in Fig. 1, FBG levels decreased and body weight increased starting from the sixth week, continuing thereafter. To further assess RK's therapeutic effect, we performed an OGTT and calculated AUC values. The OGTT showed RK effectively prevented blood glucose elevation, alleviating insulin resistance, which was supported by the

corresponding AUC results. The pathological changes of liver tissues were detected using H&E staining. As shown in Fig.1E, the liver tissue of the control group exhibited an intact structure with clearly distinguishable cell nuclei; the hepatocyte arrangement appeared well-organized and orderly. No signs of steatosis, vacuolar degeneration, or other obvious pathological alterations were observed. In contrast to the control group, the hepatocytes in the model group exhibited disordered cellular arrangement. Large areas of hepatocytes were edematous with blurred cell boundaries and manifested balloon-like degeneration (red arrow). Meanwhile, displacement of hepatocyte nuclei (black arrow) and infiltration of inflammatory cells (green arrow) were also detected. In the Met group, as well as the RK-H group, hepatocyte swelling was relatively mild, cellular arrangement was relatively orderly, and all the aforementioned pathological conditions were improved. Oil Red O staining also indicated reduced lipid droplet deposition following RK intervention (Fig. 1F). Given that abnormal lipid metabolism is a hallmark of T2DM, we further evaluated RK's effect on lipid profiles. After eight weeks, RK treatment significantly decreased serum TG, TC, and LDL-c levels and increased serum HDL-c (Fig. 2). Additionally, to preliminarily explore RK's therapeutic mechanisms, ferroptosis-related biochemical indices in liver tissues were measured by ELISA. RK significantly improved liver tissue levels of Fe^{2+} ($P < 0.05$), MDA ($P < 0.05$), SOD ($P < 0.01$), GSH ($P < 0.01$), and the GSH/GSSG ratio ($P < 0.05$).

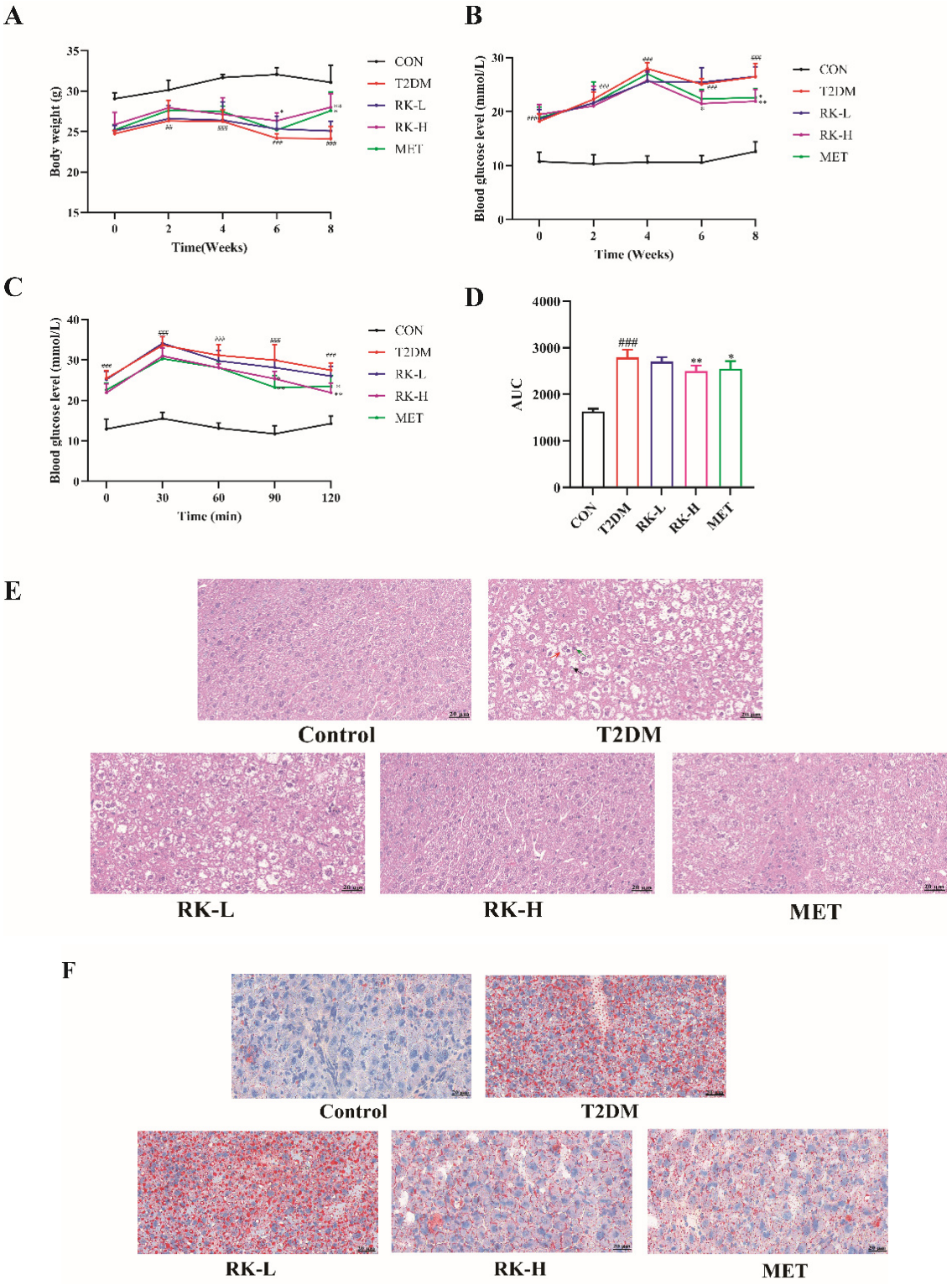

Fig. 1 Effects of RK on body weight (BW), fasting blood glucose (FBG) and glucose tolerance (OGTT, n=10), morphology and lipid droplet deposition of liver in mice of each group (n=3). (A) Body weight. (B) FBG. (C) OGTT. (D) AUC of OGTT. (E) H&E staining. (F) Oil Red O staining. Scale bar = 20 μm. Control: control group treated with vehicle per day; T2DM: type 2 diabetes mellitus (T2DM) treated with vehicle per day; RK-L: T2DM mice treated with 100 mg/kg RK per day; RK-H: T2DM mice treated with 200 mg/kg RK per day; MET: T2DM mice treated with 300 mg/kg metformin per day. Values are presented as the mean ± SEM. $^{\#}P < 0.05$, $^{\#\#}P < 0.01$, $^{\#\#\#}P < 0.001$ *vs*. Con group, $^{*}P < 0.05$, $^{**}P < 0.01$ *vs*. Model group.

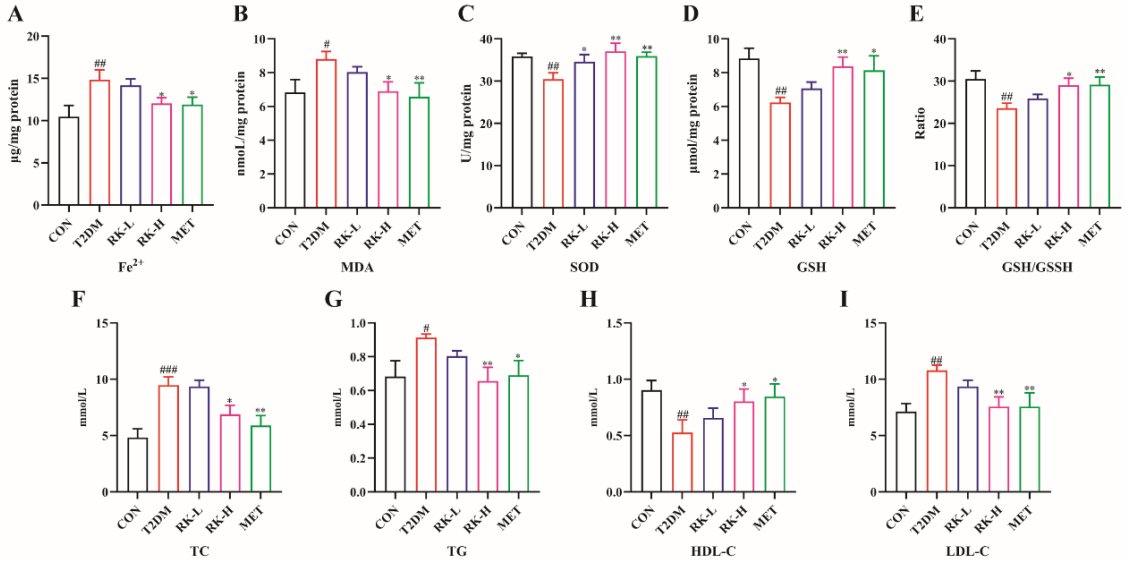

Fig. 2 Effects of RK on Fe^{2+}, MDA, SOD, GSH, GSH/GSSH ratio in liver and TC, TG, HDL-c and LDL-c in serum (n=10). Control: control group treated with vehicle per day; T2DM: type 2 diabetes mellitus (T2DM) treated with vehicle per day; RK-L: T2DM mice treated with 100 mg/kg RK per day; RK-H: T2DM mice treated with 200 mg/kg RK per day; MET: T2DM mice treated with 300 mg/kg metformin per day. Values are presented as the mean ± SEM. $^{\#}P < 0.05$, $^{\#\#}P < 0.01$, $^{\#\#\#}P < 0.001$ *vs*. Con group, $^{*}P < 0.05$, $^{**}P < 0.01$ *vs*. Model group.

3.2 RK Reduced Ferroptosis via the DJ-1/Nrf2 Pathway in Liver Tissues of T2DM Mice

The DJ-1/Nrf2 pathway plays a crucial role in ferroptosis regulation. DJ-1 promotes Nrf2 dissociation from the Nrf2-Keap1 complex, facilitating nuclear translocation and activation of downstream proteins, including NQO-1 and HO-1. Activation of these proteins induces expression of ferroptosis-inhibiting proteins GPX4 and SLC7A11, thereby reducing cell death. Therefore, we examined changes in DJ-1/Nrf2 pathway expression (Fig. 3). Expression of DJ-1 and Nrf2 proteins in the T2DM group significantly declined relative to the controls ($P < 0.001$); however, treatment with a high dosage of RK markedly elevated their expression levels ($P < 0.01$, $P < 0.05$). Additionally, RK administration counteracted the protein suppression of SLC7A11, GPX4, NQO-1, and HO-1 induced by the combined HFD and STZ regimen ($P < 0.001$). Consistent with these protein findings, mRNA quantification revealed notable downregulation of DJ-1, Nrf2, GPX4, NQO-1, and HO-1 genes due to the HFD/STZ model, whereas high-dose RK effectively restored their transcription levels. Immunohistochemical analysis further validated these observations, showing fewer DJ-1 and GPX4-positive cells in model group tissues compared to controls, with significant recovery after RK administration. Furthermore, Western blot assays indicated RK significantly enhanced anti-apoptotic Bcl-2 protein expression while reducing the pro-apoptotic protein Bax ($P < 0.05$, $P < 0.01$).

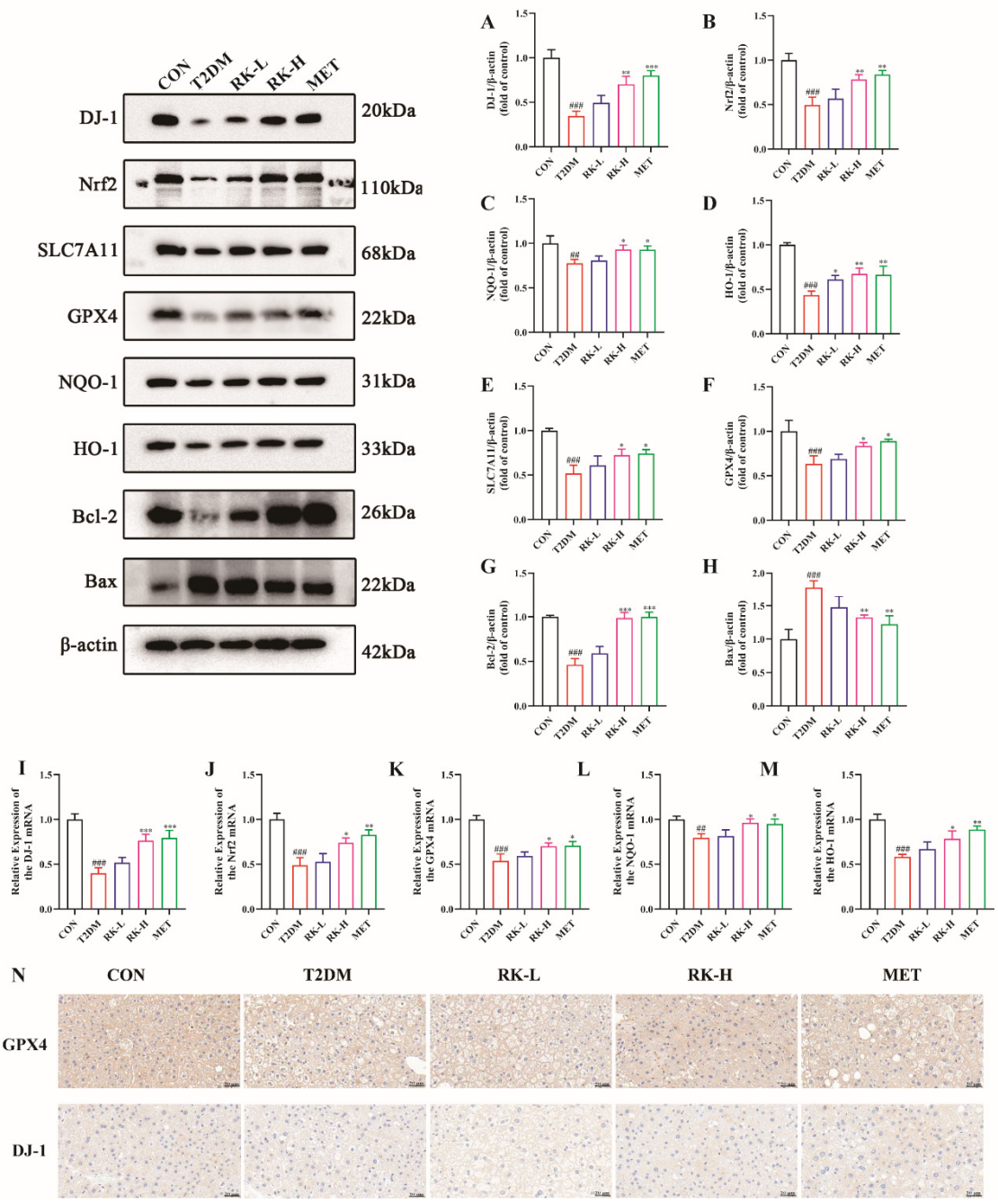

Fig. 3 Effect of RK on the ferroptosis-related protein expression in liver tissues of T2DM mice. (A-H) Representative Western blot and quantitative analysis of liver were shown. (I-M) The mRNA expression was detected by RT-qPCR. (N) Immunohistochemical detection of GPX4 and DJ-1 expression, scale bar = 20 μm. Control: control group treated with vehicle per day; T2DM: type 2 diabetes mellitus (T2DM) treated with vehicle per day; RK-L: T2DM mice treated with 100 mg/kg RK per day; RK-H: T2DM mice treated with 200 mg/kg RK per day; MET: T2DM mice treated with 300 mg/kg metformin per day. Values are expressed as mean ± SEM (n=3). $^{###}P < 0.001$ vs. Con group; $^{*}P < 0.05$, $^{**}P < 0.01$ and $^{***}P < 0.001$ *vs*. Model group.

3.3 RK Enhanced AML12 Cell Viability Reduced by OA and GLU

Imbalanced glucose and fatty acid homeostasis characterizes insulin resistance (IR), leading to ferroptosis responses. To model T2DM pathology, AML12 cells were cultured under high-glucose, high-fat (HGHF) conditions. Initially, AML12 cells were exposed to varying concentrations of GLU (0, 5, 10, 20, 40 mmol/L) or OA (0, 0.025, 0.05, 0.1, 0.2, 0.4 mmol/L) for 12 h. Reduced cell viability was observed at 10 mmol/L GLU or 0.2 mmol/L OA (Fig. 4A and B). Thus, 10 mmol/L GLU was selected as the standard

concentration to further examine OA's impact (0.1-0.3 mmol/L) on intracellular lipid droplet deposition. Optimal lipid deposition without significant cell death occurred with 0.2 mmol/L OA + 10 mmol/L GLU (Fig. 4C). Subsequently, AML12 cells were exposed to 0.2 mmol/L OA + 10 mmol/L GLU for different durations (0, 3, 6, 12, 18, 24 h) and evaluated by the CCK-8 assay. The 18 h co-culture showed decreased cell viability and significantly increased intracellular TG content (Fig. 4C and E), establishing this as the optimal modeling condition. Furthermore, RK and MET at varying concentrations were tested using the CCK-8 assay. RK (10 μmol/L) or MET (1 mmol/L) exhibited the strongest protective effects against HGHF-induced cell damage in AML12 cells (Fig. 4F-I). Collectively, our results indicated that RK and MET effectively mitigate ferroptosis in AML12 cells under HGHF conditions.

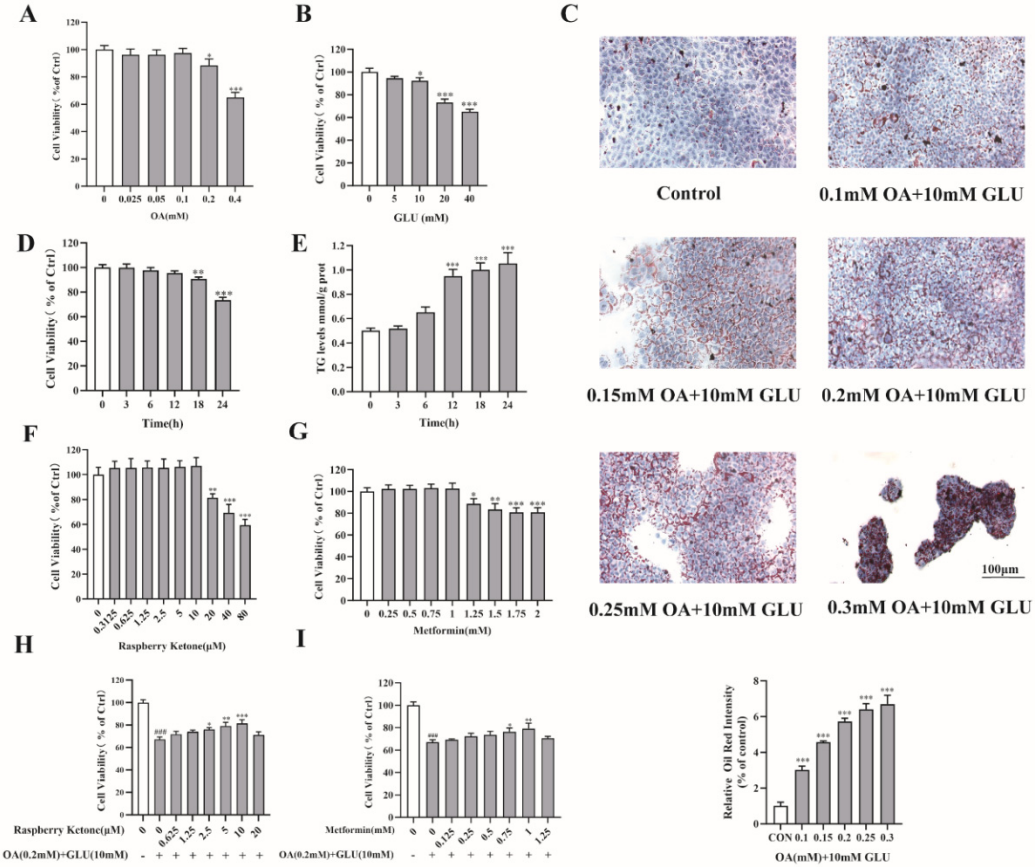

Fig. 4 Effect of RK on cell viability. (A and B) AML12 cells exposed to OA or glucose at different concentrations were assessed through a CCK-8 assay. (C) AML12 cells exposed to different concentrations of OA combined with 10 mmol/L GLU were assessed through Oil red O staining. scale bar = 100 μm. (D) AML12 cells exposed to 0.2 mmol/L OA + 10 mmol/L GLU across distinct time intervals were assessed through a CCK-8 assay. (E) The intracellular TG content was assessed through a TG kit. (F and G) AML12 cells exposed to RK or MET at different concentrations were assessed through a CCK-8 assay. (H and I) Treatment with 10 μmol/L RK or 1 mmol/L MET exhibited a pronounced protective effect in increasing cell viability against HGHF-induced AML12 cells. Values are expressed as mean ± SEM (n=3). $^{*}P < 0.05$, $^{**}P < 0.01$ and $^{***}P < 0.001$ *vs*. Con group.

3.4 RK Reduced OA and GLU-Induced Lipotoxicity in AML12 Cells

According to the above results, RK at the doses of 2.5, 5, and 10 μmol/L was selected to evaluate its protective effect against OA- and GLU-induced lipotoxicity in AML12 cells. Our results demonstrated that compared to the model group (0.2 mmol/L OA+10 mmol/L GLU), RK significantly reduced intracellular TG and TC levels in a dose-dependent manner (Fig. 5A and B). Additionally, intracellular accumulation of lipid droplets declined dose-dependently following a 6-hour RK pretreatment (Fig. 5C).

Consequently, 10 μmol/L RK was determined to be optimal for protective efficacy in subsequent experimental assays.

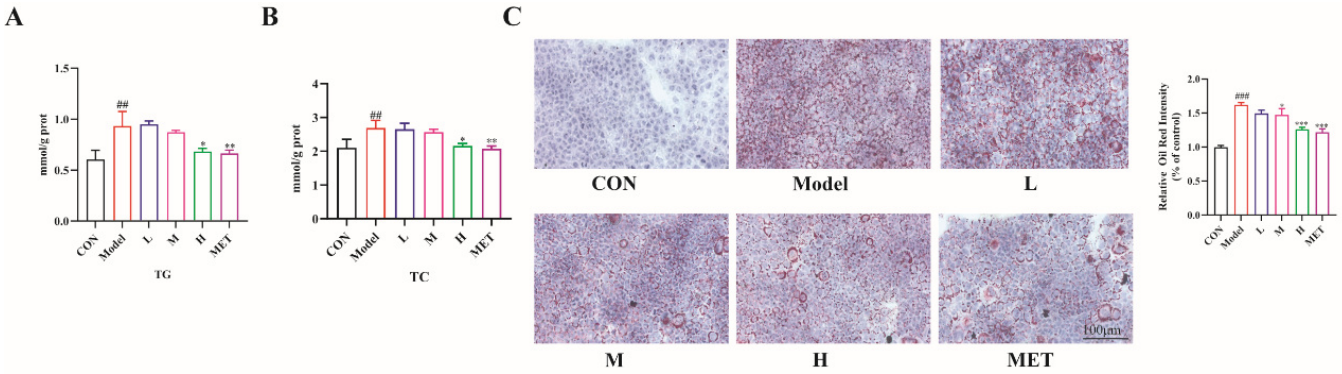

Fig. 5 Effect of RK on HGHF triggers lipotoxicity in AML12 cells. (A and B) Intracellular TG and TC content in AML12 cells. (C) Intracellular lipid droplets deposition was detected by Oil red O assay, Scale bar = 100 μm. Control: control group treated with vehicle per day; Model: AML12 cells were exposed to vehicle pretreatment for 6 h and co-incubate with 0.2 mmol/L OA + 10 mmol/L GLU for another 18 h; L: AML12 cells were exposed to 2.5 μmol/L RK pretreatment for 6 h and co-incubate with 0.2 mmol/L OA + 10 mmol/L GLU for another 18 hours; M: AML12 cells were exposed to 5 μmol/L RK pretreatment for 6 h and co-incubate with 0.2 mmol/L OA + 10 mmol/L GLU for another 18 hours; H: AML12 cells were exposed to 10 μmol/L RK pretreatment for 6 h and co-incubate with 0.2 mmol/L OA + 10 mmol/L GLU for another 18 h; MET: AML12 cells were exposed to 1 mmol/L metformin pretreatment for 6 h and co-incubate with 0.2 mmol/L OA + 10 mmol/L GLU for another 18 h. Values are presented as the mean ± SEM (n=3). $^{\#\#\#}P < 0.001$ *vs*. Con group, $^{*}P < 0.05$, $^{**}P < 0.01$, $^{***}P < 0.001$ *vs*. Model group.

3.5 RK Decreased the Occurrence of Ferroptosis

Previous studies have demonstrated that HGHF conditions enhance ROS and trigger ferroptosis. Ferroptosis is typically characterized by altered levels of ROS markers, including GSH, SOD, Fe^{2+}, MDA, and LDH. As shown in Fig. 6, elevated intracellular levels of GSH, SOD, Fe^{2+}, MDA, and LDH were observed in the model group. However, these changes were reversed after pre-treatment with RK for 6 h. Flow cytometry using DCFH-DA (ROS) probes revealed significantly increased lipid ROS levels in the model group compared with the controls. RK pre-treatment reduced lipid ROS levels in a dose-dependent manner (Fig. 6F). Additionally, BODIPY 581/591 C11 probes were used to detect lipid peroxidation by fluorescence microscopy. A color shift from red to green, indicative of lipid oxidation, was observed in the model group. RK treatment significantly reduced green fluorescence intensity and increased red fluorescence intensity in a dose-dependent manner (Fig. 6G). In summary, RK attenuates ferroptosis by reducing intracellular lipid peroxidation.

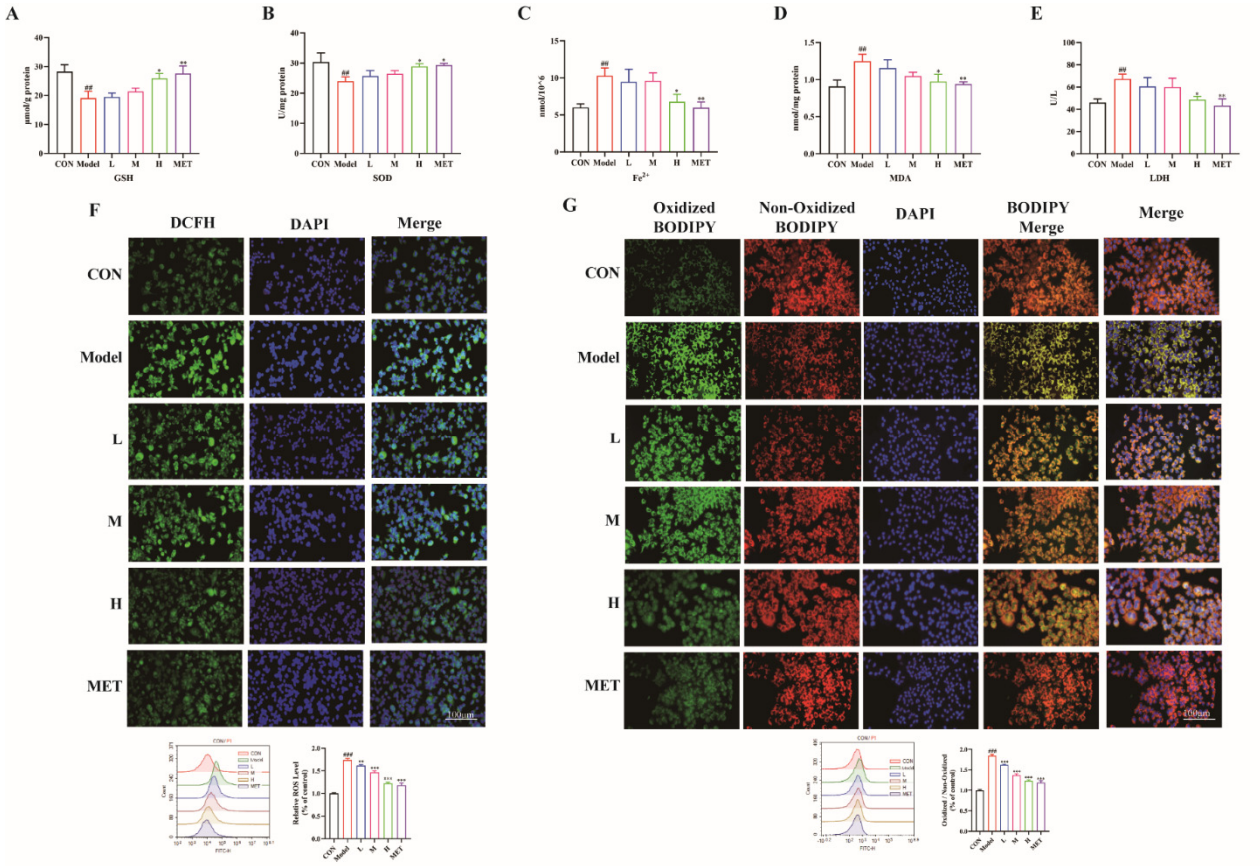

Fig. 6 Effect of RK on HGHF triggers ferroptosis in AML12 cells. (A-E) Intracellular GSH, SOD, Fe^{2+}, MDA, and LDH content in AML12 cells were detected by assay. (F) The content of intracellular lipid ROS was detected by DCFH-DA probes. (G) The content of intracellular peroxylipidates was detected by BODIPY 581/591 C11 probes. Scale bar = 100 μm. Control: control group treated with vehicle per day; Model: AML12 cells were exposed to vehicle pretreatment for 6 h and co-incubate with 0.2 mmol/L OA + 10 mmol/L GLU for another 18 h; L: AML12 cells were exposed to 2.5 μmol/L RK pretreatment for 6 h and co-incubate with 0.2 mmol/L OA + 10 mmol/L GLU for another 18 hours; M: AML12 cells were exposed to 5 μmol/L RK pretreatment for 6 h and co-incubate with 0.2 mmol/L OA + 10 mmol/L GLU for another 18 hours; H: AML12 cells were exposed to 10 μmol/L RK pretreatment for 6 h and co-incubate with 0.2 mmol/L OA + 10 mmol/L GLU for another 18 h; MET: AML12 cells were exposed to 1 mmol/L metformin pretreatment for 6 h and co-incubate with 0.2 mmol/L OA + 10 mmol/L GLU for another 18 h. Values are presented as the mean ± SEM (n=3). $^{\#\#}P < 0.01$, $^{\#\#\#}P < 0.001$ *vs*. Con group, $^{*}P < 0.05$, $^{**}P < 0.01$, $^{***}P < 0.001$ *vs*. Model group.

3.6 RK Reduced AML12 Cell Apoptosis

Annexin V-FITC and JC-1 mitochondrial membrane potential assays were employed to assess apoptosis reduction in AML12 cells by flow cytometry. As shown in Fig. 7A, medium- and high-dose RK, as well as metformin, significantly reduced apoptosis compared with the model (0.2 mmol/L OA + 10 mmol/L GLU) group. Similar findings were confirmed by JC-1 assays (Fig. 7B). Furthermore, Western blot analyses indicated that RK reduced Bax expression and enhanced Bcl-2 expression relative to the model group.

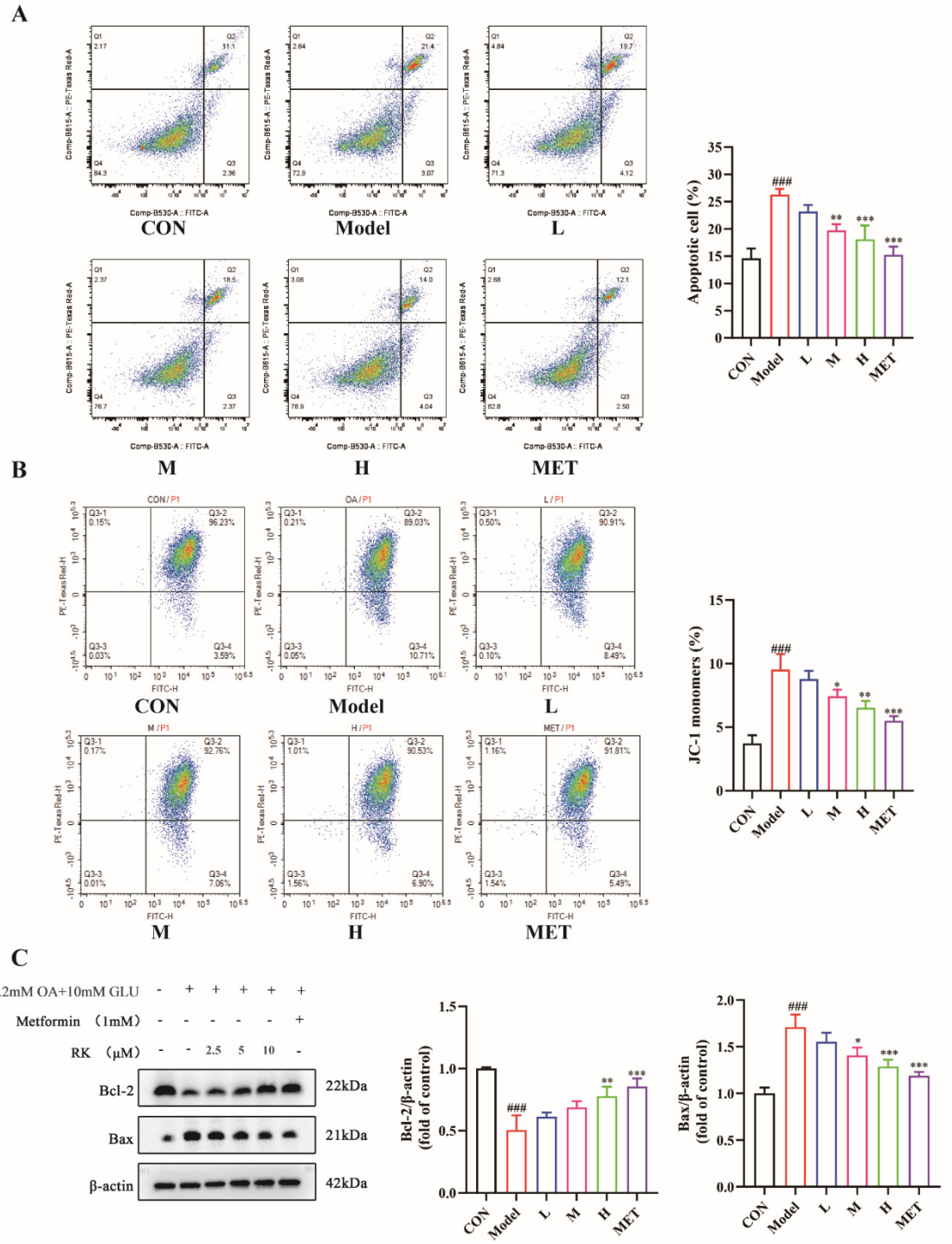

Fig. 7 Effect of RK on the apoptosis of AML 12 cells treated with HFHG. (A, B) Representative flow cytometry analysis of apoptosis and JC-1 staining. (C) Representative Western blot analysis of Bax and Bcl-2. Control: control group treated with vehicle per day; Model: AML12 cells were exposed to vehicle pretreatment for 6 h and co-incubate with 0.2 mmol/L OA + 10 mmol/L GLU for another 18 h; L: AML12 cells were exposed to 2.5 μmol/L RK pretreatment for 6 h and co-incubate with 0.2 mmol/L OA + 10 mmol/L GLU for another 18 hours; M: AML12 cells were exposed to 5 μmol/L RK pretreatment for 6 h and co-incubate with 0.2 mmol/L OA + 10 mmol/L GLU for another 18 hours; H: AML12 cells were exposed to 10 μmol/L RK pretreatment for 6 h and co-incubate with 0.2 mmol/L OA + 10 mmol/L GLU for another 18 h; MET: AML12 cells were exposed to 1 mmol/L metformin pretreatment for 6 h and co-incubate with 0.2 mmol/L OA + 10 mmol/L GLU for another 18 h. Values are presented as the mean ± SEM (n=3). $^{\#\#\#}P < 0.001$ *vs*. Con group, $^{*}P < 0.05$, $^{**}P < 0.01$, $^{***}P < 0.001$ *vs*. Model group.

3.7 RK Activated the DJ-1/Nrf2 Pathway Associated with Ferroptosis

As illustrated in Fig. 8, RK markedly upregulated protein expression of DJ-1, SLC7A11, GPX4, NQO-1, and HO-1 compared to the diabetic model group. Furthermore, RK enhanced the nuclear

localization of Nrf2 without altering its cytoplasmic expression. Similar findings were corroborated at the transcriptional level by mRNA expression analyses.

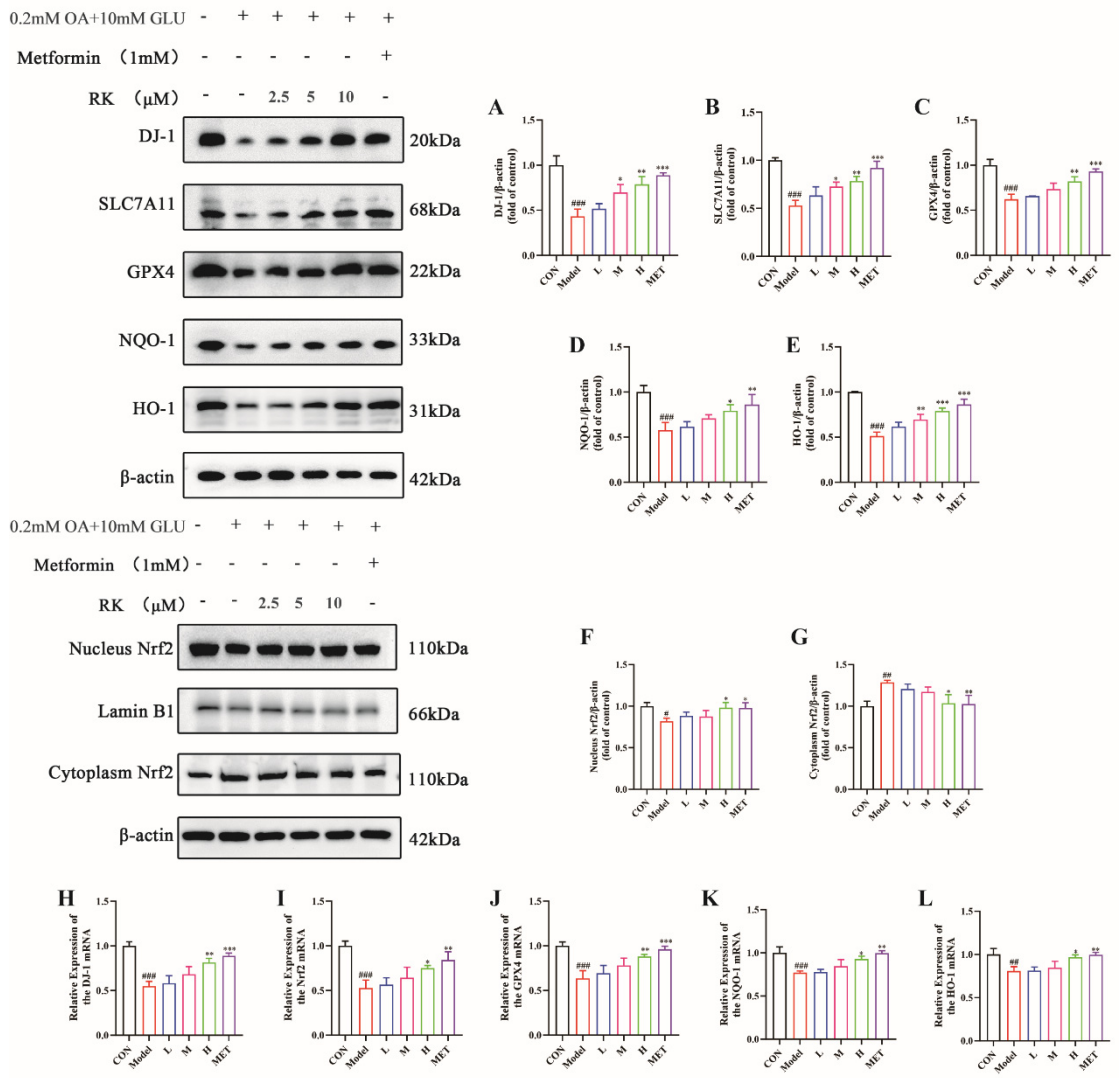

Fig. 8 Effect of RK on the DJ-1/Nrf2 signaling pathway associated with ferroptosis in AML 12 cells treated with HFHG. (A-G) Representative Western blot and quantitative analysis of AML 12 cells were shown. (H-L) The mRNA expression was detected by RT-qPCR. Control: control group treated with vehicle per day; Model: AML12 cells were exposed to vehicle pretreatment for 6 h and co-incubate with 0.2 mmol/L OA + 10 mmol/L GLU for another 18 h; L: AML12 cells were exposed to 2.5 μmol/L RK pretreatment for 6 h and co-incubate with 0.2 mmol/L OA + 10 mmol/L GLU for another 18 hours; M: AML12 cells were exposed to 5 μmol/L RK pretreatment for 6 h and co-incubate with 0.2 mmol/L OA + 10 mmol/L GLU for another 18 hours; H: AML12 cells were exposed to 10 μmol/L RK pretreatment for 6 h and co-incubate with 0.2 mmol/L OA + 10 mmol/L GLU for another 18 h; MET: AML12 cells were exposed to 1 mmol/L metformin pretreatment for 6 h and co-incubate with 0.2 mmol/L OA + 10 mmol/L GLU for another 18 h. Values are expressed as mean ± SEM (n=3). $^{###}P < 0.001$ vs. Con group; $^{*}P < 0.05$, $^{**}P < 0.01$ and $^{***}P < 0.001$ *vs*. Model group.

3.8 RK Regulated DJ-1 Signaling Pathway

DJ-1 expression was silenced by transfecting AML12 cells with DJ-1-specific siRNA. Transfection efficiency was confirmed by assessing DJ-1 protein and mRNA levels. The second siRNA, exhibiting the highest transfection efficiency, was selected for subsequent experiments (Fig. 9A). To further investigate whether RK's effects on ferroptosis-related proteins and mRNA expression depended on DJ-1/Nrf2 signaling, AML12 cells were treated with siRNA-DJ-1. The results demonstrated that DJ-1 knockdown abolished RK-induced changes in DJ-1 and downstream protein expression.

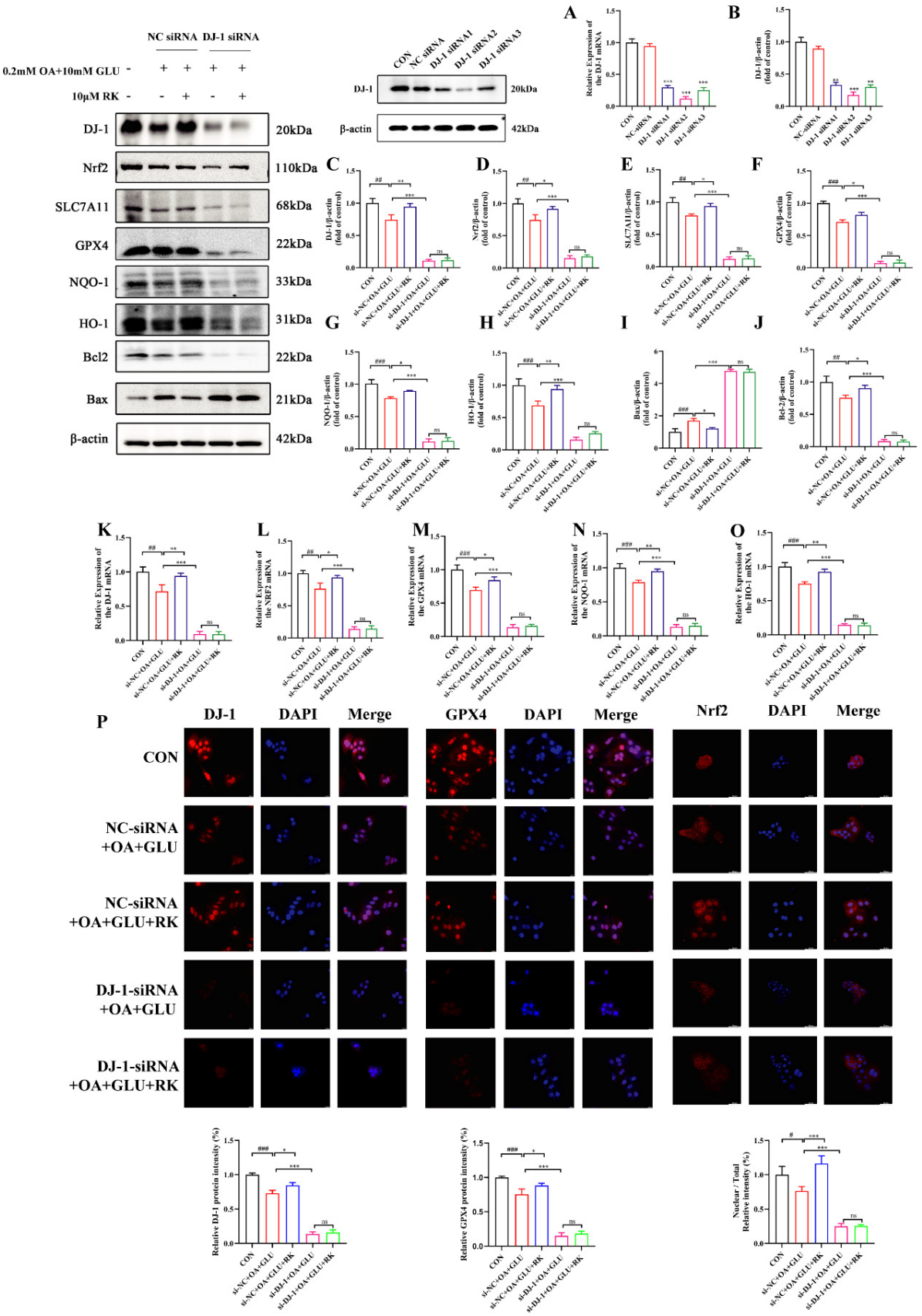

Fig. 9 Effect of RK on the target DJ-1. (A) The mRNA level of DJ-1 after treating with siRNA. (B) The protein level of DJ-1 after treating with siRNA. (C-J) The proteins of DJ-1, Nrf2, SLC7A11, GPX4, NQO-1, HO-1, Bax and Bcl-2 levels were detected by Western blot. (K-O) the expression of DJ-1, Nrf2, SLC7A11, GPX4, NQO-1 and HO-1 mRNA levels were detected by RT-qPCR. (P) The expression levels of Nrf2, DJ-1 and GPX4 were detected by immunofluorescence. Values are presented as the mean ± SD. Values are expressed as mean ± SEM (n=3). $^{\#}P < 0.05$, $^{\#\#}P < 0.01$, and $^{\#\#\#}P < 0.001$ vs. Con group; $^{*}P < 0.05$, $^{**}P < 0.01$ and $^{***}P < 0.001$ *vs*. NC si-mRNA+OA+GLU.

3.9 RK-Mediated Reduction in Lipotoxicity and Lipid Peroxidation Depended on DJ-1/Nrf2 Pathway

Firstly, we evaluated the effect of siRNA-DJ-1 on GSH, SOD, Fe^{2+}, MDA, and LDH content in AML12 cells. As shown in Fig. 10A-E, RK pre-treatment for 6 h failed to regulate the content of GSH, SOD, Fe^{2+}, MDA and LDH in siRNA-DJ-1-treated cells. Furthermore, RK pre-treatment for 6 h failed to reduce intracellular lipid droplet deposition in siRNA-DJ-1-treated cells (Fig. 10F). Similar results were observed for lipid ROS and peroxidation levels (Fig. 10G and H).

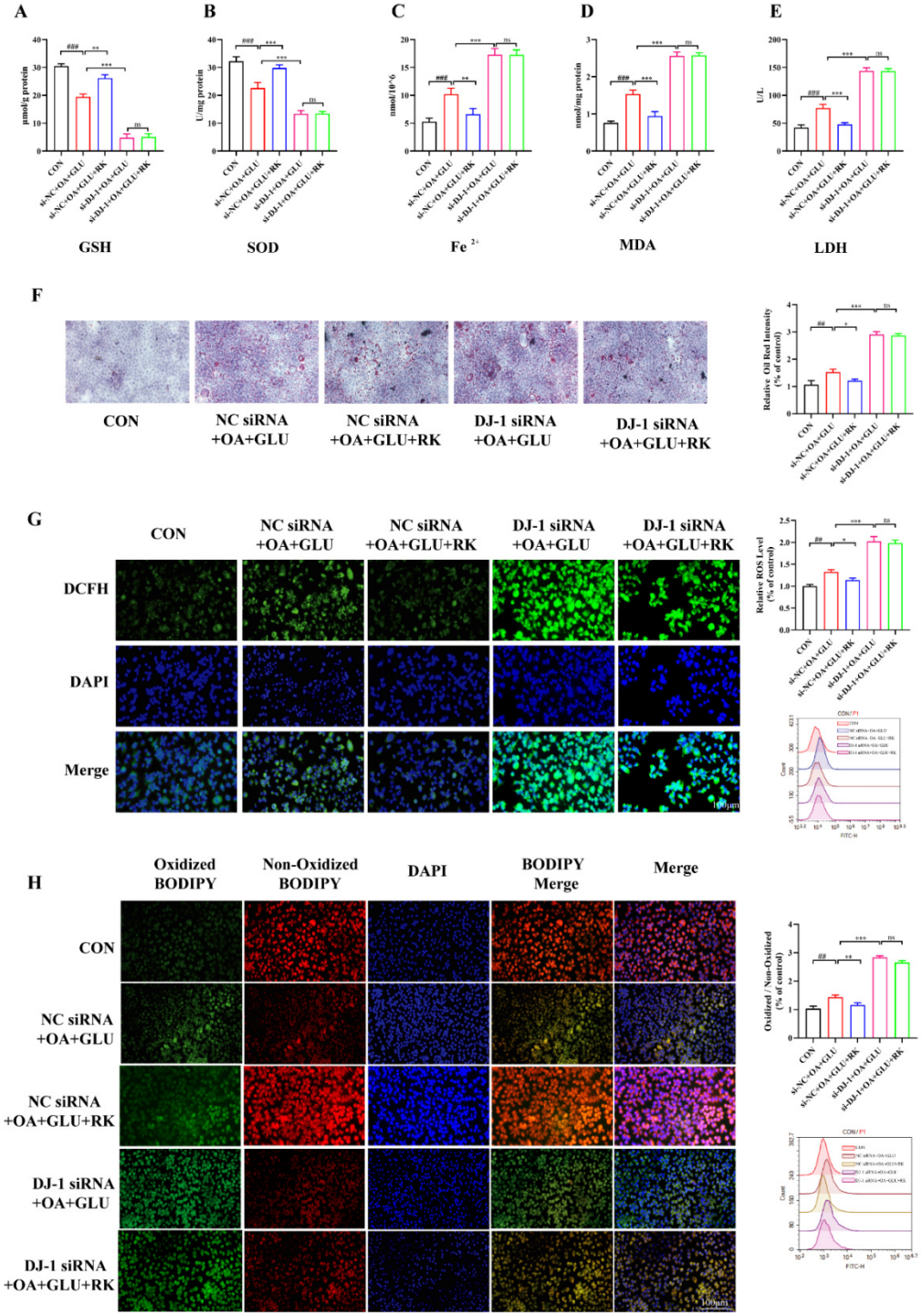

Fig. 10 Effect of RK on HGHF triggers ferroptosis by treating siRNA. (A-E) Intracellular GSH, SOD, Fe^{2+}, MDA, and LDH content in siRNA-DJ-1-treated AML12 cells were detected by assay. (F) Intracellular lipid droplet was detected by Oil red O assay, Scale bar = 100 μm. (G)The content of ROS was detected by DCFH-DA probes. (H)The content of lipid peroxide was detected by BODIPY 581 / 591 C11 probes. Scale bar = 100 μm. Values are presented as the mean ± SEM (n=3). $^{\#\#}P < 0.01$, $^{\#\#\#}P < 0.001$ vs. Con group, $^{*}P < 0.05$, $^{**}P < 0.01$, $^{***}P < 0.001$ *vs.* NC siRNA+OA+GLU.

3.10 RK Directly Interacted with DJ-1

To verify whether RK directly interacts with DJ-1, CETSA and DARTS assays were performed. In the CETSA experiment, DJ-1 protein melting curves shifted rightward in RK-treated samples compared with vehicle-treated controls (Fig. 11A). Moreover, DJ-1 protein stability increased with elevated RK concentrations at 60 ℃ (Fig. 11B). Consistent with CETSA results, DARTS assays also confirmed direct interactions between RK and DJ-1 (Fig. 11C). Mechanistically, we hypothesized that Nrf2, in addition to transcriptional activation, might physically interact with SLC7A11 to further regulate its activity. Therefore, co-IP assays were performed in HEK293T cells without RK treatment, and the results demonstrated a direct interaction between DJ-1 and Nrf2 (Fig. 11D), supporting the predictions generated by AlphaFold 3 (Fig. 11E).

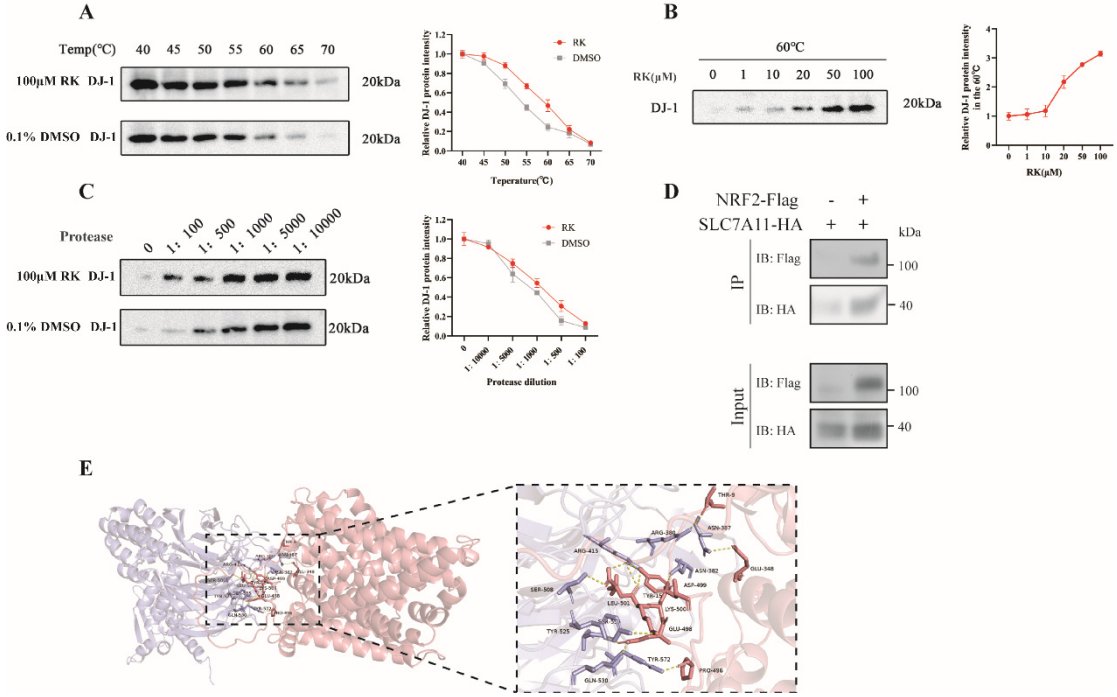

Fig. 11 RK acts directly on the DJ-1 target. (A) The level of DJ-1 protein expression after treating at different temperatures with RK. (B) The level of DJ-1 protein expression after treating different concentrations of RK at 60 ℃. (C) The level of DJ-1 proteins expression after treating different concentrations of protease with RK. (D) Co-IP analysis showing the interaction between NRF2 and SLC7A11 in HEK293T cells under RK-untreated conditions. (E) Structural prediction of the NRF2–SLC7A11 interaction generated by AlphaFold 3. The intensity of SLC7A11 or Nrf2 was detected by Western blot. Values are presented as the mean ± SEM (n=3).

4. Discussion

Although the pathogenesis of T2DM has been extensively studied over the past four decades, it remains incompletely understood. Abnormal lipid metabolism is considered an important factor in T2DM progression [26]. Disrupted lipid metabolism leads to abnormal intracellular accumulation of FFAs, subsequently increasing lipid peroxidation products. Excessive accumulation of iron-dependent lipid peroxidation products triggers ferroptosis and lipid ROS production [27, 28]. Although significant progress has been made in elucidating ferroptosis's role in T2DM pathogenesis, no effective anti-ferroptosis drugs are currently approved for T2DM treatment [29]. RK, a highly abundant aromatic phenolic compound in red raspberries, has garnered increasing attention due to its efficacy and safety in hepatoprotection [21, 30]. Accumulating evidence

demonstrates RK's antioxidant activity and ability to improve metabolic profiles in a zebrafish hyperglycemia model [31]. The present study explored RK's effects on OA- and glucose-induced injury in AML12 cells and in an HFD/STZ-induced T2DM mouse model. Our results indicated that RK ameliorates T2DM-associated lipotoxicity by modulating ferroptosis and lipid ROS via the DJ-1/Nrf2 pathway.

Hepatic glucose production accounts for approximately 90% of endogenous glucose production and is crucial for systemic glucose homeostasis. During fasting states, the liver provides glucose through glycogenolysis and gluconeogenesis to maintain normal blood sugar levels and supply energy substrates for cells [32]. After meals, the liver reduces intestinal glucose absorption into the bloodstream by enhancing glycogen synthesis, promoting glycolysis, and inhibiting hepatic glucose output. Therefore, the liver is critically involved in T2DM development and progression. Under physiological conditions, the liver rapidly responds to metabolic fluctuations between feeding and fasting states by glycogen breakdown, gluconeogenesis inhibition, and insulin secretion regulation [33]. However, substantial evidence shows liver damage in T2DM patients, characterized by dyslipidemia-elevated serum TC, TG, and LDL-c, and reduced HDL-c levels. Consistent with findings by Jiang et al. [34], our study demonstrated that RK alleviated liver injury and reduced lipid droplet deposition. Furthermore, RK supplementation reversed pathological elevations of TC, TG, and LDL-c, and elevated HDL-c levels. Liver injury frequently coincides with insulin resistance (IR), disrupting glucose homeostasis. IR improvement is an essential indicator for therapeutic efficacy in T2DM interventions [35]. Our findings demonstrated that RK effectively restored insulin signaling and improved glucose tolerance in an HFD/STZ-induced IR model, thereby enhancing intracellular signaling pathways related to insulin secretion.

Ferroptosis is primarily driven by an imbalance between oxidative and antioxidant reactions, characterized by abnormal accumulation of ferric ions and ROS generated through lipid peroxidation [36]. MDA, a hallmark of lipid peroxidation, is a critical mediator of cellular oxidative stress damage, while excessive ROS production ultimately triggers ferroptotic cell death [37]. Additionally, reduced mitochondrial membrane potential and lysosomal overflow are typical features of ferroptotic cells. Here, our results demonstrated that RK suppressed iron accumulation in AML12 cells and liver tissues. Notably, RK intervention significantly decreased ROS levels, reduced MDA production, lipid droplet deposition, and lysosomal overflow, and improved mitochondrial membrane potential in AML12 cells and the T2DM model. Furthermore, ferroptosis-related biochemical indicators, such as SOD, GSH, and GSH/GSSG ratio, were evaluated. Our results confirmed that RK increased intracellular SOD and GSH levels and improved the GSH/GSSG ratio in AML12 cells and liver tissues. These findings collectively suggest that RK inhibits hepatic ferroptosis in vitro and in vivo. Since ROS, MDA, SOD, and GSH are critical oxidative stress biomarkers, our study also implies that RK alleviates oxidative damage in hepatocytes under lipotoxic conditions. Ferroptosis is known to induce pore formation in plasma or organelle membranes through lipid peroxidation products, ultimately leading to cell death [38]. Bax activation accelerates apoptosis, whereas Bcl-2

inhibits apoptosis by interacting with pro-apoptotic mitochondrial proteins. Our data demonstrated that RK treatment reduced apoptosis by downregulating Bax and upregulating Bcl-2 expression.

Although the precise mechanisms underlying ferroptosis require further clarification, emerging evidence highlights GPX4 as central to iron metabolism and ferroptosis regulation [39, 40]. Nrf2, a nuclear transcription factor, typically remains in the cytoplasmic bound to Kelch-like ECH-associated protein-1 (Keap1), maintaining low activity via ubiquitination and proteasomal degradation under physiological conditions [41]. Under pathological stress, Keap1 activity is inhibited, allowing Nrf2 dissociation and rapid nuclear translocation, where it binds to ARE [42, 43]. The nuclear Nrf2-ARE complex regulates downstream targets, including HO-1, NQO-1, and GPX4, reducing lipid peroxidation and lipid ROS accumulation [44-46]. Accumulating studies indicate Nrf2 alleviates insulin resistance and hepatic fibrosis in T2DM by suppressing oxidative damage and ferroptosis [47]. Thus, we measured protein levels of Nrf2, HO-1, NQO-1, and GPX4 in AML12 cells and liver tissues using Western blot. RK treatment restored the expression of these proteins. Immunofluorescence analyses further confirmed that RK promoted Nrf2 nuclear translocation. Recent reports suggest GPX4 synthesis depends on the Xc^- system (comprising SLC7A11 and SLC3A2), with Nrf2 critically activating SLC7A11. However, no prior studies have reported direct interactions between Nrf2 and SLC7A11 [48]. We verified their interaction through co-IP assays, confirming direct binding between the two proteins. Moreover, structural predictions using AlphaFold3 identified strong binding sites between Nrf2 and SLC7A11, consistent with our co-IP findings. These results further support the critical role of their interaction in regulating oxidative stress, providing a structural basis for understanding their functional relationship.

The redox protein DJ-1 functions as a crucial signaling molecule regulating Nrf2 activity [11,49]. DJ-1 directly enhances molecular chaperone activity, inhibits p53 mitochondrial translocation to sustain ATP production, and mediates downstream signaling pathways such as Nrf2/GPX4 to stimulate SOD and GSH production. To further clarify the molecular mechanisms underlying RK's protective effects against lipotoxicity and ferroptosis, DJ-1 expression was assessed using Western blot and RT-qPCR. Our results indicated significantly increased DJ-1 expression in AML12 cells and T2DM models following RK intervention. Additionally, siRNA, CETSA, and DARTS assays confirmed direct interactions between RK and DJ-1. Collectively, these findings demonstrate that RK alleviates lipotoxicity and ferroptosis in vitro and in vivo by activating the DJ-1/Nrf2 pathway.

Several limitations exist in our study. Firstly, the effect of DJ-1 overexpression on hepatocytes was not examined. Secondly, due to the absence of specific ferroptosis biomarkers, the study relied primarily on measurements of intracellular ROS, MDA, and mitochondrial membrane potential. Finally, DJ-1 knockout models were not established in vivo to validate RK's therapeutic effects. Future investigations incorporating comprehensive ferroptosis biomarkers and DJ-1 knockout models would strengthen our findings.

In summary, our results suggest that RK effectively mitigates IR and lipotoxicity via the ferroptosis-related DJ-1/Nrf2 pathway (Fig. 12). This study provides evidence supporting RK as a potential therapeutic agent for T2DM treatment.

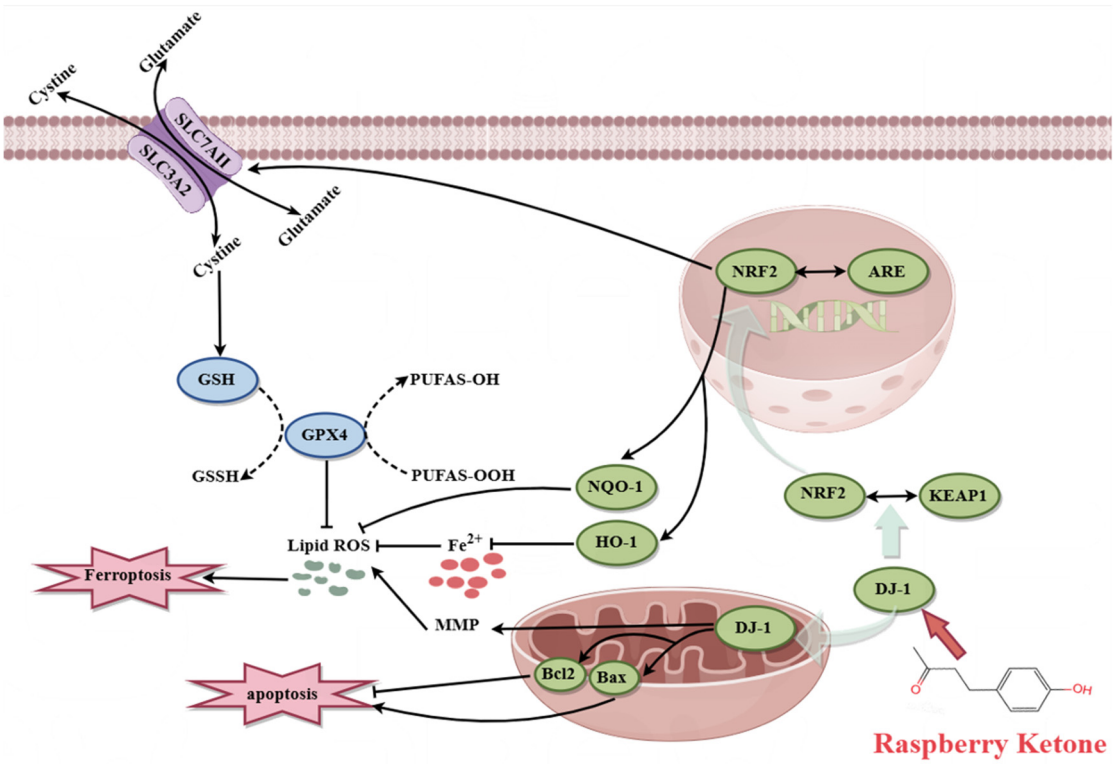

Fig. 12 Molecular mechanism of RK in the treatment of T2DM

5. Conclusion

This study demonstrated RK's protective effects against T2DM-associated lipotoxicity in liver tissues and clarified its mechanism using molecular biology, computational biology, and biophysical techniques. RK inhibited ferroptosis and apoptosis by activating the DJ-1/Nrf2 pathway, thereby alleviating liver injury in T2DM.

Declaration of competing interest

The authors declare that they have no known competing financial interests or personal relationships that could have appeared to influence the work reported in this paper.

Acknowledgments

The research was supported by the Natural Science Foundation of China (32400581, 82405007 and 82400911) and the Natural Science Foundation of Jiangxi province (20224BAB216120, 20232BAB206159, 2024QNJJL0491, 20232BAB206041 and 20232BAB215026).

References

[1] M. Viprey, Y. F. Xue, A. Rousseau, et al., Adherence with brand versus generic bisphosphonates among osteoporosis patients: a new-user cohort study in the French National Healthcare Insurance database, Sci. Rep. 10 (2020) 7446. https://doi: 10.1038/s41598-020-64214-x.

[2] N. G. Shita, A. S. Iyasu, Glycemic control and its associated factors in type 2 diabetes patients at Felege Hiwot and Debre Markos referral hospitals, Sci. Rep. 12 (2022) 9459. https://doi:10.1038/s41598-022-13673-5.

[3] D. M. Muoio, C. B. Newgard, Mechanisms of disease: Molecular and metabolic mechanisms of insulin resistance and beta-cell failure in type 2 diabetes, Nat. Rev. Mol. Cell. Biol. 9 (2008) 193-205. https://doi:10.1038/nrm2327.

[4] J. M. Baena-Díez, J. Peñafiel, I. Subirana, et al., Risk of cause-specific death in individuals with diabetes: a competing risks analysis, Diabetes Care 39 (2016) 1987-1995. https://doi.org/10.2337/dc16-0614.

[5] R. Liu, J. Wang, Y. Zhao, et al., Study on the mechanism of modified Gegen Qinlian decoction in regulating the intestinal flora-bile acid-TGR5 axis for the treatment of type 2 diabetes mellitus based on macro genome sequencing and targeted metabonomics integration, Phytomedicine 132 (2024) 155329. https://doi:10.1016/j.phymed.2023.155329.

[6] C. Y. Xu, C. Xu, Y. N. Xu, et al., Poliumoside protects against type 2 diabetes-related osteoporosis by suppressing ferroptosis via activation of the Nrf2/GPX4 pathway, Phytomedicine 125 (2024) 155342. https://doi:10.1016/j.phymed.2024.155342.

[7] M. M. Ghazaly, G. E. Lee, N. L. Ma, et al., A review and a bibliometric analysis of tropical herbs and their bioactive compounds for modulating gut microbiota function and glucose regulation in type 2 diabetes, Food & Medicine Homology 2 (2025) 9420068. https://doi.org/10.26599/FMH.2025.9420068.

[8] F. Li, Y. Shen, Q. Chen, et al., Therapeutic effect of ketogenic diet treatment on type 2 diabetes, Journal of Future foods 2-2 (2022) 177-183. https://doi.org/10.1016/j.futfo.2022.03004.

[9] F. S. A. Saadeldeen, Y. Niu, H. Wang, et al., Natural products: regulating glucose metabolism and improving insulin resistance. Food Sci. Hum. Well. 9 (2020) 214-228. https://doi. org/10.1016/j.fshw.2020.04.005.

[10] J. D. Li, T. Q. Wang, P. P. liu, et al., Hesperetin ameliorates hepatic oxidative stress and inflammation via the PI3K/AKT-Nrf2-ARE pathway in oleic acid-induced HepG2 cells and a rat model of high-fat diet-induced NAFLD, Food Funct. 12 (2021) 3898-3918. https://doi. org/10.1039/d0fo02736g.

[11] R. Pradhan, H. Yin, O.H.Y. Yu, et al., Incretin-based drugs and the risk of acute liver injury among patients with type 2 diabetes, Diabetes Care 45 (2022) 2289-2298. https://doi. org/10.2337/dc22-0712.

[12] N. Sasaki, R. Maeda, R. Ozono, et al., Early-phase changes in serum free fatty acid levels after glucose intake are associated with type 2 diabetes incidence: The hiroshima study on glucose metabolism and cardiovascular diseases, Diabetes Care 45 (2022) 2309-2315. https://doi:10.2337/dc21-2554.

[13] X. L. Zhang, J. N. Qiu, F. F. Huang, et al., Type 2 diabetes mellitus makes corneal endothelial cells vulnerable to ultraviolet a-induced oxidative damage via decreased DJ-1/Nrf2/NQO1 pathway, Invest. Ophthalmol. Vis. Sci. 63 (2022) 25. https://doi:10.1167/iovs.63.12.25.

[14] Y. Ding, Q. N. Wu, 1, 25D/VDR inhibits pancreatic β cell ferroptosis by downregulating FOXO1 expression in diabetes mellitus, Cell. Signal. 105 (2023) 110564. https://doi:10.1016/j.cellsig.2022.110564.

[15] P. Strzyz, Iron expulsion by exosomes drives ferroptosis resistance, Nat. Rev. Mol. Cell Biol. 21 (2020) 4-5. https://doi:10.1038/s41580-019-0195-2.

[16] S. Doll, M. Conrad, Iron and ferroptosis: a still ill-defined liaison, IUBMB Life. 69 (2017) 423-434. https://doi:10.1002/iub.1616.

[17] J. Cao, X. B. Chen, L. Jiang, et al., DJ-1 suppresses ferroptosis through preserving the activity of S-adenosyl homocysteine hydrolase, Nat. Commun. 11 (2020) 1251. https://doi:10.1038/s41467-020-15109-y.

[18] Y. Yuan, Y. Y. Zhai, J. J. Chen, et al., Kaempferol ameliorates oxygen-glucose deprivation/reoxygenation-induced neuronal ferroptosis by activating Nrf2/SLC7A11/GPX4 axis, Biomolecules 11 (2021) 923. https://doi:10.3390/biom11070923.

[19] D. Y. Zhao, B. Yuan, D. Kshatriya, et al., Influence of diet-induced obesity on the bioavailability and metabolism of raspberry ketone (4-(4-Hydroxyphenyl)-2- Butanone) in mice, Mol. Nutr. Food Res. 64 (2020) e1900907. https://doi.org/10.1002/mnfr.201900907.

[20] L. Bredsdorff, E. B. Wedebye, N. G. Nikolov, et al., Raspberry ketone in food supplements--High intake, few toxicity data--A cause for safety concern? Regul. Toxicol. Pharmacol. 73(2015) 196-200. https://doi.org/10.1016/j.yrtph.2015.06.022.

[21] Y. K. Liu, C. L. Dai, C. D. Wang, et al., Raspberry ketone prevents LPS-induced depression-like behaviors in mice by inhibiting TLR-4/NF-κB signaling pathway via the gut-brain axis, Mol. Nutr. Food Res. 68 (2024) e2400090. https://doi.org/10.1002/mnfr.202400090.

[22] X. P. Li, T. Wei, M. Wu, et al., Potential metabolic activities of raspberry ketone, J. Food Biochem. 46 (2022) e14018. https://doi.org/10.1111/jfbc.14018.

[23] E. T. Mehanna, B. M. Barakat, M. H. ElSayed, et al., An optimized dose of raspberry ketones controls hyperlipidemia and insulin resistance in male obese rats: Effect on adipose tissue expression of adipocytokines and Aquaporin 7, Eur. J. Pharmacol. 832 (2018) 81-89. https://doi:10.1016/j.ejphar.2018.05.028.

[24] S. L. Xiong, L. M. Yue, G. T. Lim, et al., Inhibitory effect of raspberry ketone on α-glucosidase: docking simulation integrating inhibition kinetics, Int. J. Biol. Macromol. 113 (2018) 212-218. https://doi:10.1016/j.ijbiomac.2018.02.124.

[25] R. T. Attia, Y. A. Mottaleb, D. M. Abdallah, et al., Raspberry ketone and Garcinia Cambogia rebalanced disrupted insulin resistance and leptin signaling in rats fed high fat fructose diet, Biomed. Pharmacother. 110 (2019) 500-509. https://doi:10.1016/j.biopha.2018.11.079.

[26] R. A. DeFronzo, Pathogenesis of type 2 diabetes mellitus, Med. Clin. 88 (2004) 787-835. https://doi:10.1016/j.mcna.2004.04.013.

[27] D. L. Tang, X. Chen, R. Kang, et al., Ferroptosis: molecular mechanisms and health implications, Cell Res. 31 (2021) 107-125. https://doi:10.1038/s41422-020-00441-1.

[28] M. J. Guo, X. L. Huang, J. H. Zhang, et al., Palmitic acid induces β-cell ferroptosis by activating ceramide signaling pathway, Exp. Cell Res. 440 (2024) 114134. https://doi:10.1016/j.yexcr.2024.114134.

[29] G. P. Guan, J. Liu, Q. Zhang, et al., NFAT5 exacerbates β-cell ferroptosis by suppressing the transcription of PRDX2 in obese type 2 diabetes mellitus, Cell Mol. Life Sci. 82 (2025) 64. https://doi:10.1007/s00018-024-05563-y.

[30] C. Morimoto, Y. Satoh, M. Hara, et al., Anti-obese action of raspberry ketone, Life Sci. 77 (2002) 194-204. https://doi:10.1016/j.lfs.2004.12.029.

[31] X. L. Zhu, D. C. Zhang, Y. Wang, et al., Study on the signaling pathways involved in the anti-hyperglycemic effect of raspberry ketone on zebrafish using integrative transcriptome and metabolome analyses, Food Funct. 15 (2024) 9457-9470. https://doi:10.1039/d4fo01675k.

[32] Z. H. Dong, R. Y. Pan, G. Y. Ren, et al., A novel antidiabetic peptide GPAGAP from Andrias davidianus collagen hydrolysates: screening, action mechanism prediction and improving insulin resistance in HepG2 cells, Food & Medicine Homology 1(2024) 9420010. http://dx.doi.org/10.26599/FMH.2024.9420010.

[33] V. G. Athyros, M. Doumas, K. P. Imprialos, et al., Diabetes and lipid metabolism, Hormones (Athens). 17 (2018) 61-67. https://doi:10.1007/s42000-018-0014-8.

[34] Y. C. Jiang, J. Y. Dou, M. Y. Xuan, et al., Raspberry Ketone attenuates hepatic fibrogenesis and inflammation via regulating the crosstalk of FXR and PGC-1α signaling, J. Agric. Food Chem. 72 (2024) 15740-15754. https://doi:10.1021/acs.jafc.4c03286.

[35] Z. Z. Liao, J. Y. Zhang, B. Liu, et al., Polysaccharide from okra (*Abelmoschus esculentus* (L.) Moench) improves antioxidant capacity *via* PI3K/AKT pathways and Nrf2 translocation in a type 2 diabetes model, Molecules 24 (2019) 1906. https://doi:10.3390/molecules24101906.

[36] X. Jiang, B. R. Stockwell, M. Conrad, Ferroptosis: mechanisms, biology and role in disease, Nat. Rev. Mol. Cell Biol. 22 (2021) 266-282. https://doi:10.1038/s41580-020-00324-8.

[37] D. D. Zheng, J. Liu, H. L. Piao, et al., ROS-triggered endothelial cell death mechanisms: focus on pyroptosis, parthanatos, and ferroptosis, Front. Immunol. 13 (2022) 1039241. https://doi:10.3389/fimmu.2022.1039241.

[38] W. X. Sha, F. Hu, Y. Xi, et al., Mechanism of ferroptosis and its role in type 2 diabetes mellitus, J. Diabetes Res. 28 (2021) 9999612. https://doi:10.1155/2021/9999612.

[39] Z. Qu, J. C. Sun, W. N. Zhang, et al., Transcription factor NRF2 as a promising therapeutic target for Alzheimer's disease, Free Radic. Biol. Med. 159 (2020) 87-102. https://doi:10.1016/j.freeradbiomed.2020.06.028.

[40] L. M. D. Plano, G. Calabrese, M. G. Rizzo, et al., The role of the transcription factor Nrf2 in alzheimer's disease: therapeutic opportunities, Biomolecules 13 (2023) 549. https://doi:10.3390/biom13030549.

[41] S. O. Rahman, T. Khan, A. Iqubal, et al., Association between insulin and Nrf2 signalling pathway in Alzheimer's disease: a molecular landscape, Life Sci. 328 (2023) 121899. https://doi:10.1016/j.lfs.2023.121899.

[42] J. Xiao, C. G. Luo, A, M. Li, et al., Icariin inhibits chondrocyte ferroptosis and alleviates osteoarthritis by enhancing the SLC7A11/GPX4 signaling, Int. Immunopharmacol. 133 (2024) 112010. https://doi:10.1016/j.intimp.2024.112010.

[43] P. C. Xu, B. F. Lin, X. H. Deng, et al., VDR activation attenuates osteoblastic ferroptosis and senescence by stimulating the Nrf2/GPX4 pathway in age-related osteoporosis, Free Radic. Biol. Med. 193 (2020) 720-735. https://doi:10.1016/j.freeradbiomed.2022.11.013.

[44] M. J. Kerins, A. Ooi, The roles of NRF2 in modulating cellular iron homeostasis, Antioxid. Redox Sign. 29 (2018) 1756-1773. https://doi:10.1089/ars.2017.7176.

[45] C. Tonelli, I. I. C. Chio, D. A. Tuveson, Transcriptional regulation by Nrf2, Antioxid. Redox Sign. 29 (2018) 1727-1745. https://doi:10.1089/ars.2017.7342.

[46] X. Y. Zhang, Z. X. Ji, Q. He, et al., Gegen Qinlian Decoction inhibits liver ferroptosis in type 2 diabetes mellitus models by targeting Nrf2, J. Ethnopharmacol. 340 (2025) 119290. https://doi:10.1016/j.jep.2024.119290.

[47] J. X. Song, J. R. An, Q. Chen, et al., Liraglutide attenuates hepatic iron levels and ferroptosis in db/db mice, Bioengineered 13 (2022) 8334-8348. https://doi:10.1080/21655979.2022.2051858.

[48] S. C. Lu, Regulation of glutathione synthesis, Mol. Aspects Med. 30 (2009) 42-59. https://doi:10.1016/j.mam.2008.05.005.

[49] S. S. Zhang, X. Liu, J. H. Wang, et al., Targeting ferroptosis with miR-144-3p to attenuate pancreatic β cells dysfunction via regulating USP22/SIRT1 in type 2 diabetes, Diabetol. Metab. Syndrome. 14 (2022) 89. https://doi:10.1186/s13098-022-00852-7.